#### **OPEN ACCESS**



# A Population of Compact Radio Variables and Transients in the Radio-bright Zone at the Galactic Center Observed with the Jansky Very Large Array

Jun-Hui Zhao <sup>1</sup>, Mark R. Morris <sup>2</sup>, and W. M. Goss <sup>3</sup>, and M. Goss <sup>3</sup>

#### Abstract

Using Jansky Very Large Array data obtained from high-resolution observations at 5.5 GHz at multiple epochs in 2014 and 2019, we have detected a population of radio variables and transients in the radio-bright zone at the Galactic center. With observations covering a sky area of 180 arcmin<sup>2</sup> at an angular resolution of 0."4, we report new detections of 110 Galactic center compact radio (GCCR) sources with a size of <1". The flux densities of GCCR sources exceed 70  $\mu$ Jy, with at least  $10\sigma$  significance. Among these sources, 82 are variable or transient and 28 are nonvariable. About 10% of them are expected to be extragalactic background sources. We discuss the possible astrophysical nature of the detected sources. As compared to the Galactic disk (GD) population of normal pulsars (NPs) and millisecond pulsars (MSPs), a majority (80%) of the GCCR sources appear to fall within the high flux density tail of the pulsar distribution, as extrapolated from a sample of NPs in the GD. However, MSPs extrapolated from the GD population are too weak to have contributed significantly to the GCCR population that has been detected. We also cross-correlated the GCCR sources with X-ray sources in Chandra X-ray catalogs and found that 42 GCCR sources have candidate X-ray counterparts. Most of the GCCR sources having X-ray counterparts are likely to be associated with unresolved or slightly resolved radio jets launched from X-ray binaries with a compact object, either a black hole or a neutron star.

Unified Astronomy Thesaurus concepts: Galactic center (565); Black holes (162); Radio pulsars (1353); Millisecond pulsars (1062); Neutron stars (1108); White dwarf stars (1799); Discrete radio sources (389); Radio transient sources (2008); Interstellar medium (847); Radio continuum emission (1340); Radio interferometry (1346)

Supporting material: machine-readable table

#### 1. Introduction

The central parsecs of our Galaxy host a nuclear star cluster (NSC) with a mass of  $(2-3) \times 10^7 M_{\odot}$  (Feldmeier et al. 2014; Schödel et al. 2014). The mechanism of the formation of the NSC is not clear among the two possible scenarios that have been discussed: in situ formation (Milosavljević 2004; Aharon & Perets 2015) versus the migration of stars from a more distant region into the central parsec via the process of dynamical friction (Tremaine et al. 1975; Antonini et al. 2015; Arca-Sedda & Capuzzo-Dolcetta 2017). There is evidence that a large fraction of the cluster stars are as old (>10 Gyr) as those in the inner Galactic bar/bulge (Schödel et al. 2020), although the young massive stars at the center of the Galactic NSC (Schödel et al. 2003; Ghez et al. 2005; Genzel et al. 2010; Lu et al. 2013) demonstrate the occurrence of ongoing star formation. The high stellar density at the Galactic center (GC) and the high density of compact X-ray sources there (Zhu et al. 2018) suggest that the central parsecs likely host a large population of stellar binary systems belonging to low-mass X-ray binaries (LMXBs; Muno et al. 2005; McClintock 2006). The compact components in LMXBs are likely associated with either stellar black holes (BH-LMXBs) or neutron stars (NS-LMXBs) (Hailey et al. 2018; Zhu et al. 2018). Some of the X-ray variables found in the GC

Original content from this work may be used under the terms of the Creative Commons Attribution 4.0 licence. Any further distribution of this work must maintain attribution to the author(s) and the title of the work, journal citation and DOI.

appear to be associated with the activities occurring in BH-LMXBs (Degenaar et al. 2015; Degenaar & Wijnands 2010; Hailey et al. 2018). Some of the NS-LMXBs are thought to host ordinary or normal pulsars (NPs) and millisecond pulsars (MSPs) (Pfahl & Loeb 2004; Wharton et al. 2012). Recently, an excess of X-ray source counts at the GC has been found to be comparable in magnitude to the excess determined in globular clusters (Muno et al. 2005; Haggard et al. 2017), where a large population of NPs and MSPs has been found. <sup>4,5</sup> Consequently, one might expect the GC to host a large population of NPs and MSPs. In fact, very few have been found, leading to the wellknown "missing pulsar problem" (e.g., Kramer et al. 2000; Johnston et al. 2006; Macquart et al. 2010; Bates et al. 2011; Wharton et al. 2012; Eatough et al. 2013b; Dexter & O'Leary 2014; Macquart & Kanekar 2015; Eatough et al. 2015; Rajwade et al. 2017; Bower et al. 2018).

Based on a deep Chandra X-ray survey, Muno et al. (2004) suggested that the vast majority of the GC X-ray sources are cataclysmic variables (CVs). CVs are low-mass close binary systems consisting of a white dwarf (WD) as a primary, accreting materials lost from a Roche lobe filling, late-type companion star. In the magnetic type (mCVs), the WD primaries harbor strong magnetic fields and produce a stand-off shock above the WD surface (Aizu 1973), while the accretion flow along the magnetic field reaches supersonic velocities. The post-shock region is hot

http://www.naic.edu/pfreire/GCpsr.html

https://www.atnf.csiro.au/research/pulsar/psrcat/ (ATNF Pulsar Catalog).

 $(kT\sim 10{-}50~{\rm KeV})$  and cools via thermal bremsstrahlung radiation in hard X-rays. The hard X-ray surveys of the INTEGRAL/IBIS-ISGRI and Swift/BAT surprisingly detected 1600 sources above 20 keV (Bird et al. 2016; Oh et al. 2018). The follow-up deep X-ray observations with Chandra, XMM-Newton, and NuSTAR revealed, indeed, that a large population of intermediate polars (IPs), a type of mCVs, dominates the hard X-ray emission in the central 10 pc (Muno et al. 2004; Heard & Warwick 2013; Perez et al. 2015; Hailey et al. 2016; Hong et al. 2016).

Jet outflows often arise from dynamic interactions within accretion disks associated with BHs (e.g., Shakura & Sunyaev 1973), pulsars and MSPs in some NS systems (van den Eijnden et al. 2018), and perhaps CVs (Coppejans & Knigge 1919; Barrett et al. 2017), producing radio emission. Thus, high-resolution observations at radio wavelengths can provide substantial data for diagnosis of the activities in the accretion process surrounding these compact objects.

However, only a few relatively bright radio sources (e.g., Zhao et al. 1992; Eatough et al. 2013a) have so far been detected in the radio during their outbursts. Because of improvements of the Very Large Array (VLA) in both hardware and software for wideband operation, the enhanced JVLA sensitivity has allowed us to identify a population of compact radio sources embedded within the extended emission of the radio-bright zone (RBZ) within the Galaxy's central 15', or 35 pc.

In addition, low-frequency emission from compact sources is subject to scatter broadening. However, the discovery of the magnetar, SGR J1745-29, or PSR J1745-2900 hereafter, located just 3" from the bright compact radio source associated with the central BH, Sgr A\*, indicates that the effect of the scattering screen could be up to three orders of magnitude smaller than expected (Spitler et al. 2014; Bower et al. 2014). While the temporal scatter broadening of PSR J1745-2900 is less than expected by orders of magnitude, the angular broadening is consistent with that of Sgr A\*, suggesting that they both lie behind the same strong (angular) scattering screen. Therefore, lines of sight to Sgr A\* are still strongly scattered in the image domain. Also, the radio counterpart of the X-ray cannonball (Park et al. 2005), a possible runaway NS from the Sgr A East supernova remnant, shows a peak intensity of 0.5 mJy beam<sup>-1</sup> at 5.5 GHz with a resolution of 1", while the surrounding pulsar wind nebula (PWN) becomes slightly resolved at a resolution of 0."5 with A-array data (Zhao et al. 2013, 2020). The radio emission from MSPs is typically much weaker. Observations show that MSPs are indeed weaker than NPs, with mean values of logarithmic luminosity (log  $S_{\nu}D^2$ [mJy kpc<sup>-2</sup>]) of  $0.5 \pm 02$  for a sample of 31 MSPs located in the Galactic disk (GD) as compared to  $1.50 \pm 0.04$  for 369 NPs, where  $S_{\nu}$  is the observed flux density at 1.4 GHz and D is the distance in kpc (Taylor et al. 1993; Lorimer et al. 1995; Kramer et al. 1998). The spectra of MSPs are steep but comparable to those of NPs, with spectral index of  $\alpha \sim -1.7$ , where  $S_{\nu} \propto \nu^{\alpha}$ . Scaling the GD samples to the GC distance of 8 kpc, we expect mean values of flux density at 5.5 GHz to be 5 and 50  $\mu$ Jy at 5.5 GHz for the populations of MSPs and NPs, respectively. Such low flux density values estimated for both NPs and MSPs partially explain the difficulty in the detection of pulsars, especially of MSPs, at the GC. Given that the mean flux density for MSPs at the GC distance is close to the VLA sensitivity limit, we only expect detection of a few candidates for bright MSPs with the present capability of the VLA. Most

pulsars are polarized, with linear polarization of a few percent to 100% at 1.4 GHz (Johnston & Kerr 2018). On the other hand, the radio emission from MSPs is expected to be steady and highly polarized at lower frequencies, while weakly polarized or not polarized at  $\nu>3$  GHz (Kramer et al. 1999). The nonvariable MSP emission gives us a handle for finding the faint emission from MSPs in a high dynamic range (DR) image produced by combining VLA data observed at multiple epochs.

Based on our recent 5.5 GHz VLA observation in the A array on 2019 September 8, along with two previous observations on 2014 May 26 and 2014 May 17, we focus on searching for the relatively bright compact radio sources outside both the HII complexes of Sgr A West and Sgr A East. The HII gas in Sgr A West is associated with the circumnuclear disk (CND), and the nearby complex HII regions in Sgr A East, denoted as A, B, C, and D in Goss et al. (1985) or G-0.02-0.07 in Mills et al. (2011), are associated with ongoing formation of high-mass stars

The rest of the paper is organized as follows: Section 2 describes the observations, data reduction, and imaging used for searching for compact radio sources. Section 3, along with the Appendix, presents a catalog of the GC compact radio (GCCR) sources found in the RBZ from this search. Section 4 presents identifications of X-ray counterparts. Section 5 discusses the astrophysical implications of the GCCR sources and constraints regarding their nature, and Section 6 summarizes our conclusions.

# 2. Observations and Data Reduction

Deep observations achieving a sensitivity of a few  $\mu$ Jy beam<sup>-1</sup> are enabled at the JVLA by improvement in both hardware and software for wideband capability. Radio detections now become possible of some stellar sources at the GC such as X-ray binaries and bright pulsars. Therefore, we can constrain their natures using X-ray, infrared, and follow-up radio observations.

# 2.1. Data Sets and Calibrations

New JVLA observations in the A array were carried out on 2019 September 8 at 5.5 GHz. Along with two previous A-array observations at epochs 2014 May 26 and 2014 May 17, we have a total of three A-array data sets at 5.5 GHz. These observations were all carried out with an identical VLA standard correlator setup for wideband continuum covering 2 GHz bandwidth, with a single field pointing at a position near the geometrical center of the Sgr A East radio shell. Table 1 summarizes the three sets of *uv* data (Columns (1)–(7)).

The data reduction was carried out using the CASA<sup>7</sup> software package of the NRAO. The standard calibration procedure for JVLA continuum data was applied. J1733–1304 (NRAO 530) was used for complex gain calibrations. The flux density scale was calibrated using standard calibrators, 3C 286 (J1331+3030) and/or 3C 48 (J0137+3309). Corrections for the bandpass shape of each baseband and the delay across the 2 GHz bandwidth were determined based on the data from flux density calibrators. The accuracy of the flux density scale at the JVLA is 3%–5%, limited by the uncertainty of the flux density of the primary calibrator, Cygnus A (Perley & Bulter 2017).

R.A. (J2000) = 17:45:42.718, decl. (J2000) = -29:00:17.97

http://casa.nrao.edu

Table 1
Log of Data Sets and Images

			uv Da	ta			Images				
Project ID	Array	Band	ν (GHz)	$\Delta \nu$ (GHz)	HA Range	Epoch (day)	Weight (R)	$(\theta_{\mathrm{maj}}^{\mathrm{FWHM}} \times \theta_{\mathrm{min}}^{\mathrm{FWHM}}, \mathrm{PA})$ $(\mathrm{arcsec} \times \mathrm{arcsec}, \mathrm{deg})$	rms (μJy beam <sup>-1</sup> )		
(1)	(2)	(3)	(4)	(5)	(6)	(7)	(8)	(9)	(10)		
19A-289	A	Ca	5.5	2	$+0^h.3-+2^h.3$	2019 Sep 8	-0.25	$0.62 \times 0.23, 14$	7.5		
14A-346	A	$C^{a}$	5.5	2	$-0^{h}.5-+3^{h}.5$	2014 May 26	0	$0.58 \times 0.26, 20$	5.3		
14A-346	A	$C^a$	5.5	2	$-3^h.2-+0^h.7$	2014 May 17	0	$0.59 \times 0.23, -15$	5.8		

Note. Column (1): JVLA program code of PI: Mark Morris. Column (2): array configurations. Column (3): JVLA band code; "C" stands for the 5 GHz band. Column (4): observing frequencies at the observing band center. Column (5): bandwidth. Column (6): hour angle range for the data. Column (7): date corresponding to the image epoch. Column (8): robustness weight parameter. Column (9): FWHM of the synthesized beam. Column (10): rms noise of the image.

<sup>a</sup> Correlator setup: 64 channels in each of 16 subbands with channel width of 2 MHz.

#### 2.2. Imaging

Following the procedure for high-DR imaging that we developed recently (Zhao et al. 2019) and applying it to the Sgr A data with CASA, we have produced a deep image of the GC RBZ at 5.5 GHz with hybrid data obtained from a combination of observations with the JVLA in the A, B, and C arrays; the old VLA in D array; and the GBT in single-dish mode, providing good uv coverage between 0 and 800  $k\lambda$  (see the background image in Figure 1). The rms noise in a region far from the bright emission region Sgr A West is 2  $\mu$ Jy beam<sup>-1</sup>. The ratio of the peak intensity, 0.8 Jy beam<sup>-1</sup>, to the value of the rms noise implies a DR of 400,000:1. Indeed, the rms noise is similar to the mean 5.5 GHz flux density of MSPs at the GC, as extrapolated from the 1.5 GHz value assuming a frequency dependence of  $\sim \nu^{-1.7}$ .

However, the Sgr A West region that hosts the NSC emits a diffuse continuum with a total flux density of ~15 Jy at 5 GHz, distributed in the CND, in addition to the prominent minispiral feature (Ekers et al. 1983). The confidence level for detections of weak compact sources near a strong radio complex may be compromised because of various issues in sampling and imaging radio interferometer array data. In a study of compact sources lying within a large field covered by a single primary beam (PB), both PB attenuation and smearing effects due to both bandwidth and time averaging can produce a loss in intensity of a compact source. Corrections must be applied for the errors caused by these effects.

# 2.2.1. Contamination from Short-spacing Power

High-amplitude short-spacing visibilities produce confusion owing to the corresponding extended emission. In particular, an extended structure sampled by short baselines in highresolution imaging can emerge from the analysis of several small clumps that potentially lead to confusion in the identifications of weak compact sources. In addition, the relatively weak emission from compact radio sources is easily hidden in a bright extended emission complex, such as the Sgr A complex (see Figure 1). The high radio power at the GC may explain why only a few bright compact sources in the RBZ have so far been reported. Furthermore, owing to limitations of the available deconvolution algorithms, false compact sources may be produced by residual sidelobes of a dirty beam near a strong extended emission region. For example, the Fourier transform of a uniform disk is a 2D Airy function. A dirty image of a VLA sampled disk source is difficult to clean because of strong sidelobes and residual phase errors (e.g.,

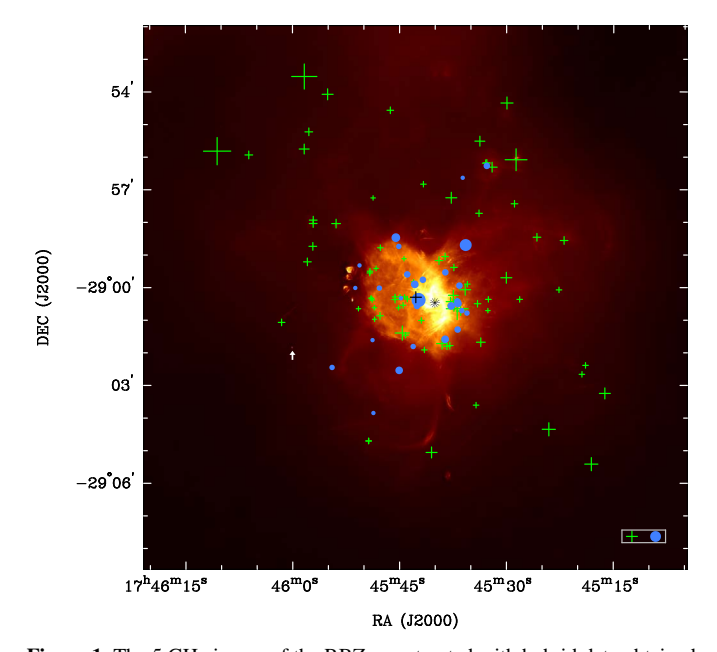
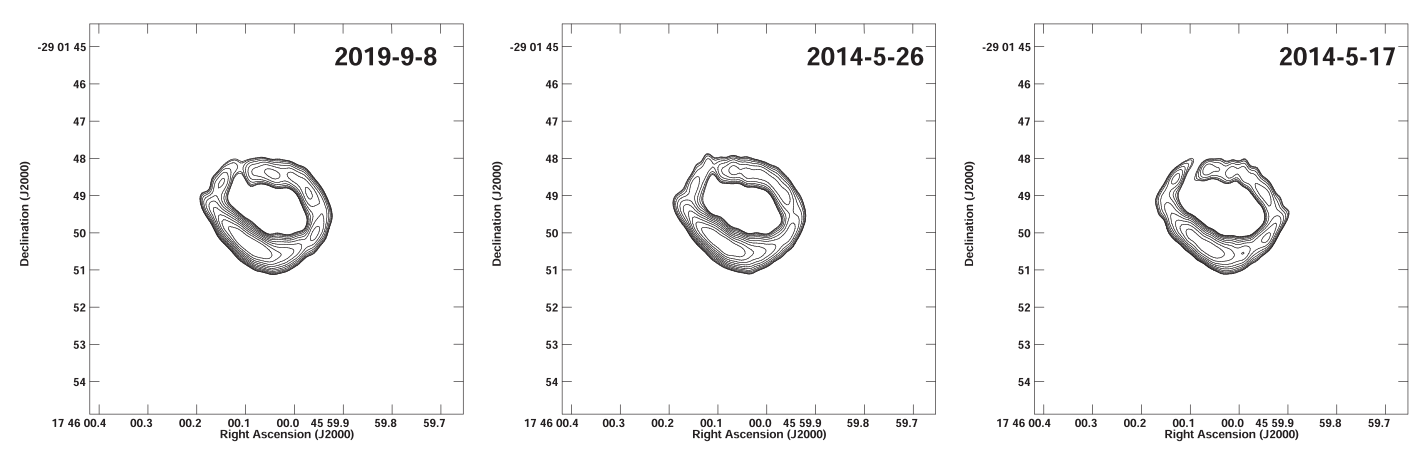


Figure 1. The 5 GHz image of the RBZ, constructed with hybrid data obtained from a combination of observations with the JVLA in the A. B. and C arrays: the old VLA in D array; and the GBT in single-dish mode, giving good uv coverage between 0 and 800 k $\lambda$ . The rms noise is  $\sim 2 \mu Jy \text{ beam}^{-1}$ synthesized FWHM beam is  $0.68 \times 0.47 \times 10^{\circ}$ . The green plus signs mark the positions of the radio variables and transients (N = 82), and the blue circles indicate the locations of nonvariables (N = 28). These GCCR sources are newly identified from the JVLA high-resolution images observed at 5.5 GHz in A array during 2014 May and 2019 September. A total of 118 compact sources are located outside Sgr A West and the HII regions A, B, C, D in Goss et al. (1985) or G-0.02-0.07 in Mills et al. (2011). The size of the symbols is scaled as  $\sim 10'' [S/1 \text{ mJy}]^{1/3}$ , where S is the source flux density. The size of the symbols in the box in the lower right corner corresponds to a 1 mJy source for both variables (plus sign) and nonvariables (circle). The Galactic plane is oriented in this figure at a position angle of  $\sim 30^{\circ}$ . A white arrow marks the location of the nebular source G-0.04-0.12 (see Figure 2 for details). The black plus sign marks the phase center of the data or the pointing center of the observations; the coordinates of the phase center are given in the text<sup>6</sup>. The black 16-pointed star marks the position of Sgr A\*.

Ledlow et al. 1992). To quantitatively evaluate the contamination from residual sidelobes of a disk source, we carried out simulations with CASA processing of visibility models using the same procedure as utilized for the real data. Three visibility data sets for a model of the diffuse disk of Sgr A West  $(75'' \times 40'', PA = 0^{\circ})$  were made, corresponding to the uv coverages sampled in each of the three epochs' observations (Table 1). We cleaned the sidelobes of the disk model with the CASA task TCLEAN and noticed that compact clumps present



**Figure 2.** The 5.5 GHz images of the nebular source G-0.04-0.12 (Mills et al. 2011) produced by filtering out the short-spacing uv data at the three epochs' observations at 2019 September 8 (left), 2014 May 26 (middle), and 2014 May 17 (right) and applying the correction for PB attenuation. The dirty images were cleaned with the MS-MSF algorithm (Rau & Cornwell 2011), and the images with cleaned components were finally convolved with a common beam of FWHM 0".50 × 0".24 (-0.005) instead of their synthesized beams. The intensities of the source observed at the three epochs can be compared without bias. Then, the difference between the levels of background emission caused by the different HA coverages of the data is correctable in the measurements of flux density (see Section 2.2.3). The total flux density of an extended source can be determined reliably in all epochs. The contours are  $1\sigma \times (10, 11, 13, 16, 20, 25, 31, 38, 46, 55, 65)$ , where the local rms noise  $\sigma = 10 \mu \text{Jy beam}^{-1}$ . The integrated flux densities of  $14.8 \pm 0.3$  mJy,  $14.6 \pm 0.3$  mJy, and  $14.7 \pm 0.3$  mJy are determined for the epochs 2019 September 8, 2014 May 26, and 2014 May 17, respectively. The source G-0.04-0.12 is marked with a white arrow in the wide field image (Figure 1), located at a distance of 3.5 from the field center, close to the contour at the half-power beam width (HPBW).

outside the disk do mimic compact radio sources up to an intensity of 0.2 mJy beam<sup>-1</sup>. These compact clumps are the sidelobes of the discrete sampling function simulated for the disk model but appear as discrete radio sources owing to the limitation in the clean process for a disk of emission. The limitation of handling the sidelobes from a complex emission source can therefore produce false compact sources.

One way to resolve this issue is to process the imaging with a cutoff of the short-baseline data that corresponds to extended emission. With the VLA A-array data at 5.5 GHz, we find that using only the longer-baseline (>100  $k\lambda$ ) data, corresponding to sampling the small-scale (<2") emission, works well for diminishing the level of the residual sidelobes. Following the same procedure described above, we cleaned the disk model with a lower baseline cutoff of 100  $k\lambda$ . The rms outside the disk in the cleaned image is improved by a factor of 15 as compared to that with all the A-array data; the maximum of the surrounding clumps drops by a factor of 100, and the rms is reduced to a level of 1  $\mu$ Jy beam<sup>-1</sup>.

This algorithm has been applied to the real data. With the three A-array data sets, we constructed images having  $20k \times 20k$  pixels covering the  $15' \times 15'$  of the RBZ region using only the longer-baseline uv data  $(>100 k\lambda)$ . The properties of the high-resolution images at the three epochs are summarized in Columns (8)–(10) of Table 1. A nebular source G-0.04-0.12 (Figure 2) with a size of  $3'' \times 4''$ , presumably with a constant flux density, is located southeast of Sgr A East (Mills et al. 2011). After filtering out the short-baseline data, the resultant image is used to verify the consistency of the flux density scale using our method. The images made from the longer-baseline data  $(>100 k\lambda)$  at the three epochs show a nearly identical ring of the nebula, demonstrating consistent images obtained with the algorithm discussed here. We find no suspected artifacts surrounding the nebular ring in the cleaned images down to a level of  $10\sigma$ .

#### 2.2.2. PB Corrections and Uncertainty

With the sensitivity of the JVLA, we are able to detect a compact source at a large radial distance from the telescope

pointing center. In a region far from the telescope pointing center, the uncertainty in the correction for attenuation becomes large. We carried out PB corrections with AIPS task PBCOR using a polynomial model updated by Perley (2016):

$$A(x) = \sum_{i=0}^{i=3} A_{2i} x^{2i},$$
 (1)

with a variable  $x = \nu r$ , where  $\nu$  is the observing frequency and r is the angular distance from the PB center, and where  $A_{2i}$  is the polynomial coefficient used in fitting the VLA PB. We corrected the image to the 2% level of the PB. At a large distance from the PB center, the corrections are subject to an increased uncertainty. The uncertainty  $\sigma_A$  of A(x) can be assessed with the formula

$$\sigma_A = \sqrt{\sum_{i=0}^{i=3} \left( \frac{\partial A(x)}{\partial A_{2i}} \sigma_{A_{2i}} \right)^2}, \qquad (2)$$

where  $\sigma_{A_{2i}}$  are the uncertainties in the polynomial coefficients  $A_0$ ,  $A_2$ ,  $A_4$ , and  $A_6$  given in Perley (2016).

#### 2.2.3. Hour Angle versus Variation of Flux Density

The variability in flux density is one of the properties that facilitates differentiating between various types of compact radio sources (e.g., Kramer et al. 2006; Brook et al. 2018; Coriat et al. 2011). Often, a compact radio source is associated with an extended emission feature surrounding an unresolved core. In such cases, the combination of intrinsic structure of a source and hour angle (HA) range in uv sampling may produce a false variability. To access the uncertainty introduced by such an effect, we simulated a linear source described by a 2D Gaussian function (0."8 × 0."1, 0° or 90°) of 0.5 mJy by adding an unresolved core, or a point source, of 0.1 mJy at the center of the linear source. With two intrinsic PA values of 0° and 90° for the linear components, 10 models of simulated linear+core sources were distributed at 10 positions at radial distances of up to 2 arcmin from the phase center to simulate

three data sets. The simulated uv data sets were made by sampling the source models in the A-array configuration with HA coverage identical to the real data, producing 128 channels covering a 2 GHz bandwidth at 5.5 GHz. Then, following the same setup and procedure as used to process the real data, the simulated data sets were Fourier-transformed by averaging every two channels, with the lower uv cutoff of 100  $k\lambda$ , and the dirty images were cleaned with CASA programs. With the AIPS task JMFIT, we made a Gaussian fit to the model sources found in the cleaned images and find that the loss in flux density is in the range of 2%-10% of the input values for the extended linear feature. The loss in peak intensity is larger for the point source, or the core, falling in the range between 30% and 65% of the input values owing to the bandwidth smearing (BWS) effect.8 The loss in peak intensity of the cores due to the BWS effect is correctable with JMFIT. For example, the correction factor  $\sqrt{1+\beta^2}$  can be computed, where  $\beta$  is provided in Equation (A4) of the Appendix.

The images of the nebula G-0.04-0.12 at three epochs made with three A-array data sets (Figure 2) were used to examine the issues of flux density variation caused by changes of HA coverage. The difference in HA coverage between the three epochs' observations does cause a minor difference in the level of a shallow negative hole underlying and surrounding an extended emission feature, although the same uv cutoff (>100  $k\lambda$ ) was consistently applied. The apparent flux densities from the positive HA images (2019 September 8 and 2014 May 26 of Figure 2) agree well with each other, while the apparent flux density derived from the 2014 May 17 image corresponding to the data taken with a negative HA coverage decreases significantly owing to a relatively deeper shallow negative area surrounding the source. The apparent flux densities integrated over the source are  $14.6 \pm 0.2$  mJy,  $14.5 \pm 0.2$  mJy, and  $11.3 \pm 0.20$  mJy determined from the images of 2019 September 8, 2014 May 26, and 2014 May 17, respectively. The corresponding values of the flux density contributed from the shallow negative hole underlying the source are  $-0.2 \pm$ 0.2 mJy,  $-0.1 \pm 0.2$  mJy, and  $-3.4 \pm 0.2$  mJy. The zero or background level biased by the HA coverage in the flux density measurements can be corrected by simply subtracting the negative flux density from the apparent source flux density. After corrections for the local negative level, the variation in the final reported flux densities of 14.8  $\pm$  0.3 mJy, 14.6  $\pm$  0.3 mJy, and  $14.7 \pm 0.3$  mJy at the three epochs for the nebula is consistent with the rms fluctuations at a level of less than 2%, similar to the uncertainties propagated from the flux density calibrations. In summary, the analysis of the nebular data verifies that a significant difference in the zero level surrounding a source is potentially present owing to differences in HA coverage for the uv data, but the bias in the determination of source flux density with Gaussian fitting is correctable with subtraction of a fitted background level using the AIPS task JMFIT automatically. Our examinations of G-0.04-0.12 images provide the procedure used for reliable measurements of the compact sources that are discussed in the rest of the paper.

Finally, we assessed a possible loss in source intensity caused by time-average smearing (TAS), using a model of circular *uv* coverage with Gaussian tapering (Bridle & Schwab 1999). We find that the fractional losses due to TAS for the sources listed in

Table 2 are less than 2% in general. For the sources located within the HPBW of the PB, the loss is less than 0.5%. Therefore, no corrections for the effect of TAS have been applied.

# 3. Catalog of Compact Radio Sources

A population of compact radio sources within the RBZ—at a level down to tens of  $\mu$ Jy—has been revealed with our 5.5 GHz VLA observations (Zhao et al. 2020). The sub-mJy compact radio sources are thought to consist of a mixture of thermal sources associated with compact/ultracompact HII regions and nonthermal synchrotron sources that are related to the particle acceleration occurring in the accretion process associated with closely interacting binary stars or perhaps with isolated pulsars and PWNs. In this paper, we primarily searched for the GCCR sources outside of the known HII regions. From the VLA A-array images observed in the three epochs, we have identified 110 compact sources located outside Sgr A West and the Sgr A East HII regions, G-0.02-0.07, but within a radius of 7.5 from the pointing center of the observations. The search criteria for the GCCR sources are based on their compactness (a size of  $\theta_{mai}$  < 1") and significance ( $S/\sigma > 10$ ).

The Appendix discusses the GCCR catalog (Table 2) in detail, along with the presentation of high-resolution images of every GCCR source at 5.5 GHz (Figure A1).

# 4. X-Ray Counterparts

# 4.1. Catalogs of X-Ray Sources and Chandra Images

Catalogs of X-ray sources in the region surrounding the GC have been produced using data from the Chandra X-Ray Observatory by combining observations taken on many different occasions (Muno et al. 2003, 2006, 2009; Zhu et al. 2018). The central Chandra pointing with the ACIS-I detector covers an area of  $17' \times 17'$ , which is comparable to the PB of the JVLA at 5.5 GHz. The Chandra field overlaps strongly with our JVLA field of view. We therefore cross-correlated our GCCR catalog with the ultradeep point-source X-ray catalog of Zhu et al. (2018), which incorporates Chandra observations between 1999 and 2013 and reports 3619 sources in the 2–8 keV band within 500" of Sgr A\*. For regions outside the Zhu et al. (2018) catalog area, we used earlier catalogs covering a greater area (Muno et al. 2008, 2009) for the cross-correlation analysis.

For candidate X-ray counterparts to GCCR sources, we also carried out a careful examination of the X-ray image used by Zhu et al. (2018) to construct their catalog. The two previously known compact X-ray and radio sources—Sgr A\* and the cannonball were used to align the coordinate frames of the X-ray and radio images. The reference centers of both images were shifted to the position of Sgr A\*: R.A.(J2000) = 17.45.40.0409, decl.(J2000) = -29:00:28.118. The precision in the positional alignment between the Chandra X-ray and JVLA images is  $\sim 0.25(S/\sigma)^{-1}$  arcsec (<0."1), where  $S/\sigma$  is the ratio of signal to noise for the reference sources used in the alignment. We found candidates using the catalog cross-correlation and then used the images to verify the coincidence and to look for possible structure in the X-ray morphology that might be helpful in assessing the correspondence. Figure 3 plots examples of those possible X-ray counterparts in  $50'' \times 50''$  subframes used in the identification process. We

This effect is proportional to  $\frac{\delta\nu}{\nu_0}$ , the ratio of channel width to the central observing frequency, and to  $r_\theta$ , the angular distance of a source to the phase center of the interferometer array (Thompson et al. 2017).

The Zhu et al. (2018) field center is at R.A.(J2000) = 17:45:40.044, decl. (J2000) = -29:00:28.04, which is displaced by  $36\rlap.{''}40$  from the JVLA pointing center.

Table 2
Catalog of Compact Radio Sources at 5.5 GHz

ID	R.A.(J2000) Decl.(J2000)	$r_{ heta}$	$\Delta \alpha$	$\Delta\delta$	$\mathscr{F}_{\mathrm{PB}}$	$\sigma \mathcal{F}_{\mathrm{PB}}^{-1}$	$\mathit{S} \pm \sigma$	$\mathit{S} \pm \sigma$	$S\pm\sigma$	$\sigma_{ m map}$	Note	es
(1)	(2)	(arcsec) (3)	(4)	(5)	(6)	(7)	(mJy) (8)	(mJy) (9)	(mJy) (10)	$(\mu \text{Jy bm}^{-1})$ (11)	r-morph (12)	x-II (13
							2019 Sep 08	2014 May 26	2014 May 17			
Variables and												
GCCR001	17:46:10.570-28:55:49.08	453.8	400.6	279.0	42	6.6	$17.2 \pm 0.8$	$7.29 \pm 0.3$	< 4.67	300	u-core	У
GCCR002	17:46:06.132-28:55:56.09	403.7	342.4	272.0	11	1.0	< 0.2	$0.40 \pm 0.03$	< 0.31	35	u-core	n
GCCR003	17:46:01.547-29:01:04.21	251.4	282.1	-36.1	2.2	0.03	$0.23 \pm 0.02$	$0.15 \pm 0.02$	$0.14 \pm 0.02$	13	u-core	n
GCCR004	17:45:58.370-28:55:45.28	341.4	240.5	282.8	5.1	0.23	$0.87 \pm 0.07$	$0.68 \pm 0.06$	$0.58 \pm 0.06$	33	u-core	У
GCCR005	17:45:57.717-28:55:13.67	362.4	232.0	314.4	6.5	0.37	$0.47 \pm 0.04$	$0.30 \pm 0.03$	$0.36 \pm 0.03$	33	u-core	n
GCCR006	17:45:58.348-28:53:31.86	455.0	240.3	416.3	45	7.1	$12.5 \pm 0.9$	$2.68 \pm 0.25$	$1.86 \pm 0.18$	300	u-core	n
GCCR007	17:45:57.931-28:59:12.88	209.9	234.7	75.2	1.7	0.017	$0.55 \pm 0.03$	$0.40 \pm 0.02$	$0.47 \pm 0.02$	13	c-core <sup>1</sup>	n
GCCR008	17:45:57.165-28:58:44.37	211.5	224.7	103.7	1.7	0.018	$0.47 \pm 0.03$	$0.28\pm0.02$	$0.30 \pm 0.02$	13	u- core	n
GCCR009	17:45:57.117-28:58:02.35	232.6	224.0	145.8	2.0	0.025	$0.42 \pm 0.04$	$0.34 \pm 0.04$	$0.25\pm0.04$	14	c-core <sup>2</sup>	n
GCCR010	17:45:57.107-28:57:56.17	236.1	223.9	151.9	2.0	0.027	$0.46\pm0.04$	$0.41\pm0.04$	$0.32\pm0.03$	14	c-core <sup>3</sup>	n
GCCR011	17:45:55.082-28:54:04.61	407.1	197.4	383.5	12	1.1	$1.20 \pm 0.11$	< 0.05	< 0.07	50	u-core	n
GCCR012	17:45:53.901-28:58:02.45	199.8	181.8	145.7	1.6	0.014	$0.63 \pm 0.04$	$0.56\pm0.04$	$0.74\pm0.05$	34	l-core <sup>4</sup>	n
GCCR013	17:45:50.764-29:00:39.19	107.8	140.7	-11.1	1.1	0.004	$0.09 \pm 0.01$	$0.05\pm0.01$	$0.06 \pm 0.01$	13	u-core	n
GCCR014	17:45:49.359-29:04:42.47	278.5	122.2	-254.4	2.8	0.061	$0.21 \pm 0.01$	$0.12 \pm 0.01$	$0.11 \pm 0.01$	20	u-core	У
GCCR015	17:45:49.330-29:04:42.41	278.3	121.8	-254.3	2.7	0.060	$0.19 \pm 0.01$	$0.15\pm0.01$	$0.16 \pm 0.01$	20	u-core	3
GCCR016	17:45:49.174-28:59:33.27	95.8	119.8	54.8	1.1	0.004	$0.18 \pm 0.01$	$0.15\pm0.01$	$0.14 \pm 0.01$	7	t-core <sup>5</sup>	r
GCCR017	17:45:49.153-28:59:30.03	97.1	119.5	58.1	1.1	0.004	$0.17 \pm 0.01$	< 0.11	< 0.10	7	d-core <sup>6</sup>	r
GCCR018	17:45:49.034-29:00:19.57	82.9	118.0	8.5	1.1	0.004	$0.10 \pm 0.02$	< 0.03	$0.10 \pm 0.01$	9	c-core <sup>7</sup>	r
GCCR019	17:45:48.908-29:00:19.99	81.2	116.3	8.1	1.1	0.003	$0.10 \pm 0.01$	$0.08 \pm 0.01$	$0.07 \pm 0.01$	7	c-core <sup>8</sup>	r
GCCR020	17:45:48.837-29:00:23.07	80.5	115.4	5.0	1.1	0.003	$0.11 \pm 0.01$	$0.10 \pm 0.02$	$0.06 \pm 0.01$	7	u-core	1
GCCR021	17:45:48.711-28:57:15.33	198.8	113.8	192.8	1.6	0.014	$0.08 \pm 0.02$	$0.07 \pm 0.02$	< 0.10	7	u-core	1
GCCR022	17:45:48.525-29:00:37.25	78.6	111.3	-9.1	1.1	0.003	$0.08 \pm 0.01$	$0.08 \pm 0.01$	$0.05\pm0.01$	6	u-core	r
GCCR023	17:45:48.508-29:00:58.51	86.1	111.1	-30.4	1.1	0.004	$0.08 \pm 0.01$	$0.10 \pm 0.01$	$0.04 \pm 0.01$	7	u-core	n
GCCR024	17:45:48.291-28:59:25.02	90.2	108.2	63.1	1.1	0.004	$0.09 \pm 0.01$	< 0.02	< 0.03	7	u-core	n
GCCR025	17:45:47.740-29:00:52.12	74.2	101.0	-24.0	1.1	0.003	$0.23 \pm 0.02$	$0.16 \pm 0.02$	< 0.05	5	c-core9	r
GCCR026	17:45:47.696-28:58:47.00	112.0	100.4	101.1	1.2	0.004	$0.16 \pm 0.01$	$0.13 \pm 0.02$	$0.10 \pm 0.01$	7	c-core <sup>10</sup>	n
GCCR027	17:45:46.300-28:54:34.08	347.1	82.1	354.0	5.4	0.26	$0.30 \pm 0.03$	< 0.07	< 0.06	25	u- core	r
GCCR028	17:45:45.638-29:00:17.43	38.3	73.4	10.7	1.0	0.003	$0.14 \pm 0.01$	$0.10 \pm 0.01$	$0.12 \pm 0.01$	10	c-core <sup>11</sup>	r
GCCR029	17:45:45.638-29:00:22.31	38.5	73.4	5.8	1.0	0.003	$0.31 \pm 0.01$	$0.31 \pm 0.01$	$0.40 \pm 0.02$	12	1-core <sup>12</sup>	r
GCCR030	17:45:45.151-29:00:37.45	37.4	67.0	-9.3	1.0	0.003	$0.15 \pm 0.01$	$0.12 \pm 0.01$	$0.10 \pm 0.01$	9	c-core <sup>13</sup>	r
GCCR031	17:45:44.932-29:00:17.14	29.0	64.2	11.0	1.0	0.003	$0.10 \pm 0.01$	$0.07\pm0.01$	$0.06 \pm 0.01$	6	c-core <sup>14</sup>	У
GCCR032	17:45:44.622-29:01:23.93	70.5	60.1	-55.8	1.1	0.003	$2.23 \pm 0.01$	$2.48 \pm 0.01$	$2.34 \pm 0.01$	13	c-core <sup>15</sup>	3
GCCR033	17:45:44.500-29:00:32.75	27.7	58.5	-4.6	1.0	0.003	$0.19 \pm 0.02$	$0.13 \pm 0.01$	$0.09 \pm 0.01$	7	c-core <sup>16</sup>	r
GCCR034	17:45:44.382-28:59:07.15	74.1	56.9	81.0	1.1	0.003	$0.07 \pm 0.01$	$0.14 \pm 0.01$	$0.10 \pm 0.01$	7	c-core <sup>17</sup>	r
GCCR035	17:45:44.300-29:00:17.56	20.8	55.9	10.6	1.0	0.003	$0.12 \pm 0.01$	< 0.02	< 0.02	10	u-core	3
GCCR036	17:45:44.172-29:01:27.87	72.5	54.2	-59.8	1.1	0.003	$0.20 \pm 0.01$	$0.11 \pm 0.02$	< 0.04	8	c-core <sup>18</sup>	3
GCCR037	17:45:43.916-29:00:21.27	16.0	50.8	6.8	1.0	0.003	$0.25 \pm 0.02$	$0.17 \pm 0.02$ $0.17 \pm 0.02$	$0.17 \pm 0.02$	10	c-core <sup>19</sup>	у
GCCR038	17:45:43.036-28:59:49.60	28.7	39.3	38.5	1.0	0.003	$0.10 \pm 0.01$	$0.20 \pm 0.02$	$0.17 \pm 0.02$ $0.15 \pm 0.02$	10	c-core <sup>20</sup>	У
GCCR039	17:45:42.623-29:00:24.80	6.9	34.3	3.3	1.0	0.003	$0.17 \pm 0.02$	$0.20 \pm 0.02$ $0.22 \pm 0.02$	$0.30 \pm 0.02$	10	c-core <sup>21</sup>	y 1
GCCR040	17:45:41.950-29:01:00.78	44.0	25.0	-32.7	1.0	0.003	$0.17 \pm 0.02$ $0.20 \pm 0.02$	$0.22 \pm 0.02$ $0.38 \pm 0.02$	$0.30 \pm 0.02$ $0.35 \pm 0.02$	13	c-core <sup>22</sup>	1
GCCR040	17:45:41.664-28:56:50.09	208.3	21.3	218.0	1.7	0.003	$0.20 \pm 0.02$ $0.22 \pm 0.02$	< 0.03	<0.03 <0.03	10	c-core <sup>23</sup>	у
GCCR041 GCCR042	17:45:41.522-29:01:54.82	98.1	19.4	-86.7	1.1	0.004	$0.13 \pm 0.01$	$0.09 \pm 0.01$	$0.08 \pm 0.01$	10	u-core	y n
GCCR042 GCCR043	17:45:40.515-29:05:03.65	287.1	6.2	-275.5	3.0	0.004	$1.04 \pm 0.03$	$1.05 \pm 0.03$	$0.90 \pm 0.03$	24	c-core <sup>24</sup>	1

Table 2 (Continued)

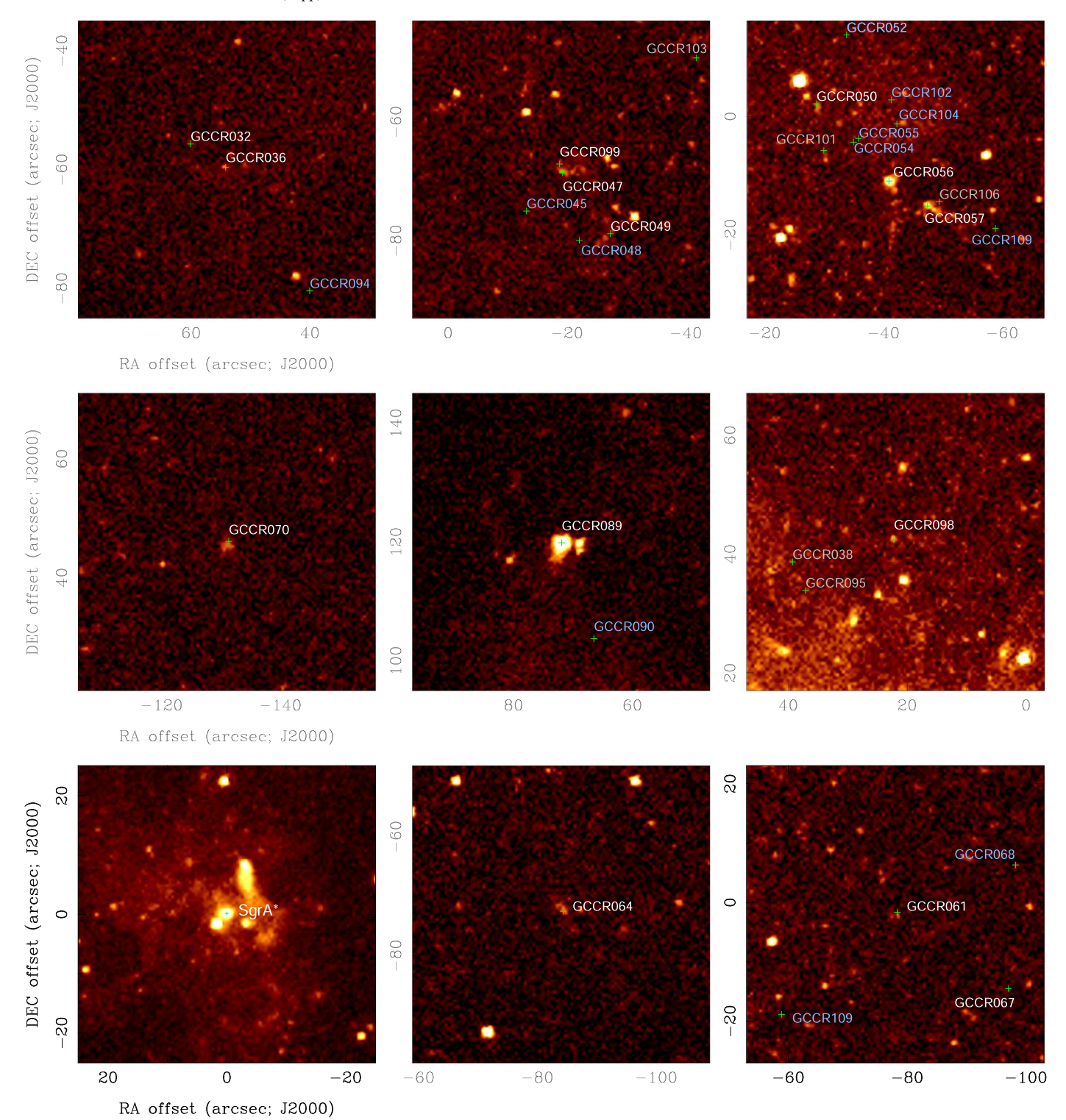
D	R.A.(J2000) Decl.(J2000)	$r_{ heta}$	$\Delta \alpha$	$\Delta \delta$	$\mathcal{F}_{\mathrm{PB}}$	$\sigma \mathcal{F}_{\mathrm{PB}}^{-1}$	$S \pm \sigma$	$S\pm\sigma$	$S\pm\sigma$	$\sigma_{ m map}$	Note	es
		(arcsec)	(arc				(mJy)	(mJy)	(mJy)	$(\mu \text{Jy bm}^{-1})$	r-morph	x-II
1)	(2)	(3)	(4)	(5)	(6)	(7)	(8)	(9)	(10)	(11)	(12)	(13)
							2019 Sep 08	2014 May 26	2014 May 17			
GCCR044	17:45:39.474-28:59:10.58	79.7	-7.4	77.5	1.1	0.003	$0.49\pm0.02$	$0.50\pm0.02$	$0.38 \pm 0.02$	18	c-core <sup>25</sup>	n
GCCR045	17:45:39.034-29:01:43.24	98.0	-13.2	-75.1	1.1	0.004	$1.00 \pm 0.02$	$1.19 \pm 0.02$	$1.21 \pm 0.02$	11	t- core <sup>26</sup>	n
GCCR046	17:45:38.617-28:59:03.21	92.1	-18.7	84.9	1.1	0.004	$0.30 \pm 0.02$	$0.16 \pm 0.02$	< 0.05	13	c-core <sup>27</sup>	n
GCCR047	17:45:38.571-29:01:36.75	95.7	-19.3	-68.6	1.1	0.004	$0.32\pm0.02$	$0.34 \pm 0.02$	$0.29\pm0.01$	13	c-core <sup>28</sup>	у
GCCR048	17:45:38.358-29:01:48.19	106.8	-22.1	-80.1	1.1	0.004	$0.26 \pm 0.01$	$0.19 \pm 0.01$	$0.21 \pm 0.01$	9	c-core <sup>29</sup>	n
GCCR049	17:45:37.958-29:01:47.05	108.8	-27.3	-78.9	1.1	0.004	$0.28 \pm 0.02$	$0.37 \pm 0.03$	$0.28 \pm 0.02$	13	c-core <sup>30</sup>	У
GCCR050	17:45:37.850-29:00:26.15	64.4	-28.7	2.0	1.0	0.003	$0.66\pm0.01$	$0.97\pm0.02$	$0.94 \pm 0.02$	22	c-core <sup>31</sup>	у
GCCR051	17:45:37.753-28:57:15.07	194.2	-30.0	193.0	1.6	0.013	$1.23 \pm 0.05$	$0.92 \pm 0.04$	$1.15 \pm 0.04$	23	1-core <sup>32</sup>	n
GCCR052	17:45:37.463-29:00:14.55	69.1	-33.8	13.6	1.1	0.003	$0.89 \pm 0.02$	$0.71 \pm 0.02$	$0.97 \pm 0.02$	29	c-core <sup>33</sup>	n
CCR053	17:45:37.390-28:59:23.23	88.8	-34.8	64.9	1.1	0.004	$0.29 \pm 0.02$	$0.22\pm0.02$	$0.18 \pm 0.01$	12	t-core <sup>34</sup>	n
CCR054	17:45:37.375-29:00:32.61	71.5	-35.0	-4.5	1.1	0.003	$1.54 \pm 0.02$	$1.95 \pm 0.02$	$1.82 \pm 0.02$	35	1-core <sup>35</sup>	n
CCR055	17:45:37.310-29:00:31.98	72.3	-35.8	-3.9	1.1	0.003	$0.84\pm0.02$	$0.78\pm0.02$	$0.56\pm0.01$	35	d-core <sup>36</sup>	n
CCR056	17:45:36.920-29:00:39.17	78.9	-40.9	-11.1	1.1	0.003	$8.16 \pm 0.03$	$8.08 \pm 0.03$	$8.40 \pm 0.03$	110	t-core <sup>37</sup>	у
CCR057	17:45:36.425-29:00:43.37	86.3	-47.4	-15.3	1.1	0.004	$0.66 \pm 0.02$	$0.62 \pm 0.02$	$0.54 \pm 0.02$	13	t-core <sup>38</sup>	у
CCR058	17:45:35.804-29:00:04.13	91.6	-55.6	24.0	1.1	0.003	$1.28 \pm 0.02$	$1.49 \pm 0.02$	$1.49 \pm 0.02$	14	1-core <sup>39</sup>	у
CCR059	17:45:35.499-28:59:53.83	97.7	-59.6	34.3	1.1	0.004	$0.17 \pm 0.02$	$0.23 \pm 0.02$	$0.25\pm0.02$	11	c-core <sup>40</sup>	y'
CCR060	17:45:34.271-29:03:36.62	227.4	-75.7	-188.5	1.9	0.023	$0.13 \pm 0.01$	< 0.08	< 0.09	10	c-core <sup>41</sup>	n
CCR061	17:45:34.068-29:00:29.91	114.0	-78.4	-1.8	1.2	0.004	$0.24 \pm 0.02$	$0.15 \pm 0.02$	$0.19 \pm 0.02$	9	l-core <sup>42</sup>	у
CCR062	17:45:33.867-28:57:43.58	193.1	-81.0	164.5	1.6	0.013	$0.24 \pm 0.02$	$0.12 \pm 0.02$	< 0.05	9	c-core <sup>43</sup>	n
CCR063	17:45:33.749-28:55:30.85	310.3	-82.6	297.3	3.7	0.11	$0.82 \pm 0.02$	$0.60 \pm 0.02$	$0.58 \pm 0.02$	20	1-core <sup>44</sup>	n
CCR064	17:45:33.610-29:01:40.76	145.4	-84.4	-72.6	1.3	0.006	$0.66 \pm 0.02$	$0.55 \pm 0.02$	$0.60 \pm 0.02$	16	t-core <sup>45</sup>	у
CCR065	17:45:32.927-28:56:11.34	278.1	- 93.4	256.8	2.7	0.060	$0.26 \pm 0.02$	$0.14 \pm 0.02$	< 0.10	19	c-core <sup>46</sup>	n
CCR066	17:45:32.767-28:56:10.82	279.5	- 95.5	257.3	2.8	0.062	$0.35 \pm 0.02$	$0.25 \pm 0.02$	$0.20 \pm 0.02$	22	u-core	n
CCR067	17:45:32.613-29:00:42.60	134.9	- 97.4	-14.5	1.2	0.006	$0.15 \pm 0.01$	$0.08 \pm 0.01$	$0.08 \pm 0.01$	10	c-core <sup>47</sup>	у
CCR068	17:45:32.552-29:00:21.95	133.4	- 98.3	6.2	1.2	0.005	$0.18 \pm 0.01$	$0.19 \pm 0.01$	$0.14 \pm 0.01$	9	u-core	n
GCCR069	17:45:32.025-28:56:18.70	277.4	-105.2	249.4	2.7	0.059	$0.82 \pm 0.03$	$0.70 \pm 0.03$	$0.60 \pm 0.03$	24	l-core <sup>48</sup>	n
CCR070	17:45:30.031-28:59:42.17	170.3	-131.3	45.9	1.4	0.009	$1.28 \pm 0.03$	$1.11 \pm 0.03$	$1.12 \pm 0.03$	12	t-core <sup>49</sup>	y
CCR071	17:45:29.947-28:54:20.64	394.7	-132.5	367.5	10	0.83	$1.39 \pm 0.12$	< 0.16	< 0.20	48	t-core <sup>50</sup>	n
CCR072	17:45:28.892-28:57:26.02	249.9	-146.3	182.1	2.2	0.035	$0.23 \pm 0.02$	$0.15 \pm 0.01$	$0.17 \pm 0.01$	13	u-core	у
CCR073	17:45:28.671-28:56:04.94	313.0	-149.2	263.2	3.8	0.12	$8.78 \pm 0.03$	$5.85 \pm 0.03$	$7.12 \pm 0.03$	100	c-core <sup>51</sup>	y
GCCR074	17:45:28.154-29:00:21.91	190.9	-155.9	6.2	1.6	0.012	$0.18 \pm 0.01$	$0.13 \pm 0.03$	$0.12 \pm 0.03$ $0.12 \pm 0.01$	10	u-core	yʻ
CCR075	17:45:24.057-29:04:20.98	344.8	-209.6	-232.9	5.3	0.24	$1.80 \pm 0.05$	$2.20 \pm 0.09$	$1.76 \pm 0.09$	40	u-core	n
CCR076	17:45:25.740-28:58:27.60	248.5	-187.6	120.5	2.2	0.034	$0.36 \pm 0.03$	$0.25 \pm 0.02$	$0.22 \pm 0.02$	13	t-core <sup>52</sup>	n
CCR077	17:45:22.641-29:00:04.46	263.7	-228.3	23.7	2.5	0.045	$0.20 \pm 0.02$	< 0.06	< 0.06	15	1-core <sup>53</sup>	y'
CCR077	17:45:21.937-28:58:33.50	292.0	-237.5	114.6	3.1	0.079	$0.20 \pm 0.02$ $0.44 \pm 0.02$	$0.27 \pm 0.02$	$0.16 \pm 0.01$	14	c-core <sup>54</sup>	n
CCR078	17:45:19.415-29:02:39.78	337.0	-237.5 $-270.5$	-131.7	4.8	0.079	$0.44 \pm 0.02$ $0.25 \pm 0.02$	$<0.27 \pm 0.02$ <0.08	<0.10 ± 0.01	20	u-core	n
CCR079	17:45:18.921-29:02:23.32	336.4	-270.3 $-277.0$	-131.7 $-115.2$	4.8	0.20	$0.23 \pm 0.02$ $0.21 \pm 0.02$	< 0.07	< 0.08	20	u-core	n
CCR080	17:45:18.090-29:05:24.99	445.6	-277.0 $-287.9$	-296.9	30	4.3	$1.93 \pm 0.19$	$0.80 \pm 0.19$	< 0.06	120	u-core	n
CCR082	17:45:16.201-29:03:14.87	390.1	-312.7	-166.8	9.5	0.74	$1.22 \pm 0.05$	$0.98 \pm 0.05$	$0.61 \pm 0.06$	50	u-core	y
							2019 Sep 08	2014 May 26	2014 May 17			
Ionvariables							2017 Sep 06	2017 Way 20	2017 Way 17			
GCCR083	17:45:54.472-29:02:27.17	201.2	189.3	-119.1	1.6	0.015	$0.16\pm0.01$	$0.17\pm0.01$	$0.16\pm0.01$	10	u-core	n
GCCR084	17:45:51.214-29:00:00.91	112.9	146.6	27.2	1.2	0.004	$0.10 \pm 0.01$	$0.11 \pm 0.01$	$0.10 \pm 0.01$	10	u-core	n

Table 2 (Continued)

ID	R.A.(J2000) Decl.(J2000)	$r_{ heta}$	$\Delta \alpha$	$\Delta\delta$	$\mathscr{F}_{PB}$	$\sigma \mathscr{F}_{\mathrm{PB}}^{-1}$	$S \pm \sigma$	$S \pm \sigma$	$S\pm\sigma$	$\sigma_{ m map}$	Note	es
		(arcsec)	(arc	esec)			(mJy)	(mJy)	(mJy)	$(\mu \text{Jy bm}^{-1})$	r-morph	x-ID
(1)	(2)	(3)	(4)	(5)	(6)	(7)	(8)	(9)	(10)	(11)	(12)	(13)
GCCR085	17:45:50.620-28:59:19.45	119.0	138.8	68.7	1.2	0.005	0.10±0.01	$0.11 \pm 0.01$	$0.09 \pm 0.01$	7	u-core	у
GCCR086	17:45:48.794-29:01:36.89	112.2	114.8	-68.8	1.2	0.004	$0.12 \pm 0.01$	$0.14 \pm 0.01$	$0.12 \pm 0.01$	10	u-core	n
GCCR087	17:45:48.676-29:03:51.03	226.9	113.2	-202.9	1.9	0.023	$0.15\pm0.01$	$0.14 \pm 0.01$	$0.14 \pm 0.01$	11	u-core	y
GCCR088	17:45:47.834-29:00:01.23	69.2	102.2	26.9	1.1	0.003	$0.22\pm0.02$	$0.24 \pm 0.02$	$0.25\pm0.02$	10	l-core <sup>55</sup>	n
GCCR089	17:45:45.522-28:58:28.39	115.6	71.9	119.7	1.2	0.005	$0.54\pm0.02$	$0.55\pm0.02$	$0.53 \pm 0.02$	9	l-core <sup>56</sup>	y
GCCR090	17:45:45.109-28:58:44.54	98.5	66.5	103.6	1.1	0.004	$0.20 \pm 0.01$	$0.21\pm0.01$	$0.21 \pm 0.01$	9	c-core <sup>57</sup>	n
GCCR091	17:45:45.060-29:02:32.57	138.1	65.8	-124.5	1.3	0.006	$0.47\pm0.02$	$0.44 \pm 0.02$	$0.45\pm0.02$	10	c-core <sup>58</sup>	n
GCCR092	17:45:44.805-29:00:19.72	27.6	62.5	8.4	1.0	0.003	$0.09 \pm 0.01$	$0.10 \pm 0.01$	$0.10\pm0.01$	8	c-core <sup>59</sup>	y?
GCCR093	17:45:43.926-28:59:36.02	44.8	51.0	52.1	1.0	0.003	$0.24\pm0.02$	$0.20\pm0.02$	$0.19 \pm 0.02$	10	t-core <sup>60</sup>	n
GCCR094	17:45:43.094-29:01:48.66	90.8	40.0	-80.5	1.1	0.004	$0.21 \pm 0.02$	$0.20\pm0.02$	$0.22 \pm 0.02$	10	c-core <sup>61</sup>	n
GCCR095	17:45:42.869-28:59:54.39	23.7	37.1	33.7	1.0	0.003	$0.55\pm0.02$	$0.55\pm0.02$	$0.55\pm0.02$	20	l- core <sup>62</sup>	y?
GCCR096	17:45:42.570-29:00:34.19	16.3	33.2	-6.1	1.0	0.003	$0.29\pm0.02$	$0.27\pm0.02$	$0.27\pm0.02$	10	l-core <sup>63</sup>	y?
GCCR097	17:45:42.346-29:00:23.03	7.0	30.2	5.1	1.0	0.003	$2.24\pm0.07$	$2.41 \pm 0.07$	$2.44 \pm 0.07$	20	t-core <sup>64</sup>	y?
GCCR098	17:45:41.737-28:59:45.85	34.6	22.2	42.3	1.0	0.003	$0.28\pm0.02$	$0.33\pm0.02$	$0.28\pm0.02$	10	c-core <sup>65</sup>	y
GCCR099	17:45:38.610-29:01:35.31	94.3	-18.8	-67.2	1.1	0.004	$0.40 \pm 0.04$	$0.40\pm0.04$	$0.43 \pm 0.04$	13	1-core <sup>66</sup>	y?
GCCR100	17:45:38.586-28:59:32.21	70.9	-19.1	55.9	1.1	0.003	$0.23 \pm 0.01$	$0.24 \pm 0.01$	$0.23 \pm 0.01$	12	c-core <sup>67</sup>	y?
GCCR101	17:45:37.756-29:00:34.02	67.1	-30.0	-5.9	1.1	0.003	$0.39 \pm 0.02$	$0.44 \pm 0.02$	$0.39 \pm 0.02$	12	t-core <sup>68</sup>	y?
GCCR102	17:45:36.888-29:00:25.49	76.8	-41.4	2.6	1.1	0.003	$0.24 \pm 0.02$	$0.23\pm0.02$	$0.26 \pm 0.02$	11	c-core <sup>69</sup>	n
GCCR103	17:45:36.858-29:01:17.46	97.2	-41.8	-49.3	1.1	0.004	$0.24 \pm 0.02$	$0.22 \pm 0.01$	$0.22 \pm 0.01$	10	u-core	y?
GCCR104	17:45:36.818-29:00:29.54	78.2	-42.3	-1.4	1.1	0.003	$0.40 \pm 0.02$	$0.41 \pm 0.02$	$0.40 \pm 0.02$	16	c-core <sup>70</sup>	n
GCCR105	17:45:36.613-28:59:56.60	82.9	-45.0	31.5	1.1	0.004	$0.30\pm0.02$	$0.34 \pm 0.02$	$0.32 \pm 0.02$	20	c-core <sup>71</sup>	n
GCCR106	17:45:36.274-29:00:42.63	88.0	-49.4	-14.5	1.1	0.004	$0.22 \pm 0.02$	$0.23 \pm 0.02$	$0.22 \pm 0.02$	9	c-core <sup>72</sup>	y?
GCCR107	17:45:36.149-28:56:38.24	236.0	-51.1	229.9	2.0	0.027	$0.09 \pm 0.01$	$0.12 \pm 0.01$	$0.10 \pm 0.01$	9	u-core	y
GCCR108	17:45:35.730-28:58:42.00	132.8	-56.6	106.1	1.2	0.005	$1.51 \pm 0.04$	$1.58 \pm 0.04$	$1.58 \pm 0.04$	10	1-core <sup>73</sup>	n
GCCR109	17:45:35.553-29:00:47.11	98.4	-58.9	-19.0	1.1	0.004	$0.23 \pm 0.03$	$0.27\pm0.03$	$0.23 \pm 0.03$	10	1-core <sup>74</sup>	n
GCCR110	17:45:32.758-28:56:16.37	274.6	-95.4	251.8	2.7	0.056	$0.23\pm0.02$	$0.21\pm0.02$	$0.23\pm0.03$	11	u-core	y

Note. Listed below are the source sizes  $\theta_{maj} \pm \sigma$ ,  $\theta_{mim} \pm \sigma$ ,  $PA_{\Theta} \pm \sigma$  in the units of (arcsec, arcsec, deg).  $^{10}.20 \pm 0.02$ ,  $0.12 \pm 0.01$ ,  $17 \pm 5$ ;  $^{20}.63 \pm 0.10$ ,  $0.29 \pm 0.10$ ,  $34 \pm 11$ ;  $^{30}.67 \pm 0.12$ ,  $0.31 \pm 0.11$ ,  $18 \pm 10$ ;  $^{40}.96 \pm 0.05$ ,  $0.10 \pm 0.09$ ,  $148 \pm 5$ ;  $^{50}.75 \pm 0.20$ ,  $0.31 \pm 0.08$ ,  $10 \pm 13$ ;  $^{50}.71 \pm 0.10$ ,  $0.24 \pm 0.16$ ,  $108 \pm 12$ ;  $^{70}.50 \pm 0.20$ ,  $0.30 \pm 0.17$ ,  $50 \pm 30$ ;  $^{80}.57 \pm 0.12$ ,  $0.1 \pm 0.1$ ,  $71 \pm 15$ ;  $^{90}.65 \pm 0.10$ ,  $0.28 \pm 0.10$ ,  $130 \pm 10$ ;  $^{10}0.46 \pm 0.1$ ,  $0.20 \pm 0.08$ ,  $85 \pm 21$ ;  $^{11}0.32 \pm 0.05$ ,  $0.04 \pm 0.03$ ,  $15 \pm 4$ ;  $^{12}0.80 \pm 0.10$ ,  $0.21 \pm 0.04$ ,  $164 \pm 3$ ;  $^{13}0.50 \pm 0.10$ ,  $0.17 \pm 0.08$ ,  $20 \pm 13$ ;  $^{14}0.35 \pm 0.13$ ,  $2.26 \pm 0.12$ ,  $68 \pm 21$ ;  $^{15}0.37 \pm 0.03$ ,  $2.28 \pm 0.03$ ,  $160 \pm 3$ ;  $^{16}0.51 \pm 0.07$ ,  $0.24 \pm 0.03$ ,  $-4 \pm 4$ ;  $^{17}0.28 \pm 0.04$ ,  $0.23 \pm 0.02$ ,  $22 \pm 5$ ;  $^{18}0.61 \pm 0.16$ ,  $0.28 \pm 0.06$ ,  $13 \pm 8$ ;  $^{19}0.77 \pm 0.08$ ,  $0.26 \pm 0.07$ ,  $20 \pm 6$ ;  $^{20}0.50 \pm 0.10$ ,  $0.33 \pm 0.06$ ,  $174 \pm 25$ ;  $^{21}0.30 \pm 0.02$ ,  $20 \pm 0.05$ 

(This table is available in machine-readable form.)



examined as well the three Chandra images in the 2–3.3 keV, 3.3-4.7 keV, and 4.7-8 keV bands for the central  $900''^{10}$  that fully

cover the RBZ observed at 5.5 GHz for the distribution of the GCCR sources. Thus, the cross-correlation analysis between X-ray and 5.5 GHz radio is spatially complete. Identifications of X-ray counterparts to individual GCCR sources are tabulated in Table 3. Column (1) is the GCCR ID. Column (2) lists the

 $<sup>\</sup>overline{^{10}}$  https://chandra.harvard.edu/photo/2010/sgra/, where the FITS images of these bands were obtained.

 Table 3

 Identifications of Candidate X-Ray Counterparts of GCCR Sources

GCCR ID	CXOGC# or G#	SS#	$\Delta \theta_{\mathrm{X-R}}$	$S_{2-8~{ m keV}}$	Ref. <sup>a</sup>
			(arcsec)	$(10^{-7} \text{ photons cm}^{-2} \text{ s}^{-1})$	
(1)	(2)	(3)	(4)	(5)	(6)
GCCR001	J174610.5-285550		1.5	60	a
GCCR004	J174558.4-285546		1.2	3.6	a
GCCR014	J174549.3-290442		0.6	5.8	a
GCCR015	J174549.3-290442		0.5	5.8	a
GCCR031	J174544.9-290017		0.8	5.5	a
GCCR032	•••	2625	0.2	2.8	b
GCCR035	J174544.2-290018		0.7	7.5	a
GCCR036	J174544.1-290128	2594	0.5	4.5	a,b
GCCR037	J174543.9-290020		1.5	15	a
GCCR038	•••	2502	2	2.1	b
GCCR041	J174541.5-285651		1.8	1.7	a
GCCR047	G359.925-0.051			18.1	c
GCCR049	•••	1898	1	8.12-7.50	b
GCCR050		1875	1	7.4–5.6	b
GCCR056	J174536.9-290039	1767	0.2	43.0-42.2	a,b
GCCR057	G359.933-0.037			22.8	c
GCCR058	G359.941-0.029			18.7	c
GCCR059	J174535.6-285953	1617	1.6	6.44-3.60	a,b
GCCR061	J174534.0-290030	1429	0.8	4.96–4.80	a,b
GCCR064	J174533.5-290140	1375	0.4	9.10–6.17	a,b
GCCR067	J174532.6-290043	1250	1	1.28–1.20	a,b
GCCR070	J174530.0-285942	956	0.7	17.5–17.0	a,b
GCCR072	J174528.8-285726	852	0.4	4.1–3.5	a,b
GCCR073	J174528.6-285605	819	0.8	9.6–8.7	a,b
GCCR074	J174528.1-290021	774	1	3.34–1.50	a,b
GCCR077		389	1	1.12	b
GCCR082	J174516.1-290315	185	0.6	40.3–30.0	a,b
GCCR085	J174550.6-285919	3042	0.3	3.2–1.7	a,b
GCCR087	J174548.7-290350	2926	0.4	3.2–2.4	a,b
GCCR089	J174545.5-285828		0.3	170	d,a
GCCR092	J174544.6-290020		2	2.7	a
GCCR095		2477	1.9	4.23	b
GCCR096	J174542.5-290033		1.2	1.9	a
GCCR097	J174542.2-290024		1.9	3.1	a
GCCR098	J174541.7-285945	2369	0.2	6.80–6.63	a
GCCR099	G359.925-0.051			18.1	a
GCCR100	J174538.6-285933		2	1.2	a
GCCR101	J174537.6-290035	1857	1.6	10–6.0	a,b
GCCR101 GCCR103	J174536.8-290117		0.4	1.5	a,o
GCCR106	G359.933-0.037			22.8	c
GCCR107	J174536.1-285638	 1671	0.5	190–186	a,b
GCCR107 GCCR110	J174532.7-285617	1263	0.7	9.4–6.9	a,b

#### Note.

name of an X-ray source in the Chandra X-ray Observatory catalog, CXOGC#, where # stands for truncated J2000 coordinates of the source JHHMMSS.S-DDMMSS (Muno et al. 2009). In the diffuse X-ray source catalog of Muno et al. (2008), the name of an X-ray source is denoted as G#, where # stands for DDD.DDD  $\pm$  D.DDD, the Galactic coordinates in degrees. Column (3) gives the source sequential numbers (SS#) in the deep X-ray catalog of Zhu et al. (2018). Column (4) gives the angular offsets between the GCCR sources and their X-ray counterparts. Column (5) lists the 2–8 keV photon flux ( $S_{2-8 \text{ keV}}$ ) reported in the catalogs, or the range of reported fluxes (upper—lower values) (Muno et al. 2008, 2009; Zhu et al. 2018). Column (6) gives the references from which the X-ray data are used in the identifications.

In addition, notes for those GGCRs involving extended X-ray emission sources such as halos and elongated nebulae, or possessing possible IR identifications, are given in Section 4.2.

In short, a total of 42 GCCR sources have candidate X-ray counterparts; most of them (27) have a positional offset between X-ray and radio,  $\Delta\theta_{\rm X-R}$ , less than 1" or less than twice the Chandra resolution; the rest of them (15) have  $\Delta\theta_{\rm X-R}=1$ " to 2". The probability that a GCCR source has an accidental coincidence within 1" or 2", given the number of ~3900 reported X-ray sources (Muno et al. 2009; Zhu et al. 2018) lying within the area covered by our radio survey, is 1.9% or 7.7%, respectively. Thus, most of the 42 GCCR sources with candidate X-ray counterparts are likely related to the X-ray sources. The majority of the GCCR sources (68) do

<sup>&</sup>lt;sup>a</sup> References: (a) Muno et al. (2009); (b) Zhu et al. (2018); (c) Muno et al. (2008); (d) Park et al. (2005).

not have X-ray counterparts within 2". The presence or absence of a candidate X-ray identification for the individual GCCR sources is also indicated in Table 2.

#### 4.2. Notes to the X-Ray Counterparts

GCCR001.—CXOGC J174610.5-285550 (Muno et al. 2009) is offset by 1."5 from the radio source. An extended X-ray halo of size 15" surrounds the compact X-ray source in the 2.0–3.3 keV and 3.3–4.7 keV bands, but no significant X-ray emission is present in the 4.7–8 keV band.

GCCR047 is a radio source associated with a bright spot in an X-ray complex, see the top-middle panel in Figure 3. The X-ray source is listed in Muno et al. (2008) as G359.925–0.051 with a power-law spectrum of  $\Gamma=1.77$  and X-ray luminosity of  $3\times 10^{32}\,\mathrm{erg\,s^{-1}}$ ; it is one of the twenty PWN candidates within the central 20 pc (Muno et al. 2008).

GCCR056.—CXOGC J174536.9-290039 (Muno et al. 2009) is a compact X-ray source having an offset  $<0.^{\prime\prime}$ 2 from the radio source. In the deep X-ray catalog of Zhu et al. (2018), this source is listed as SS#1767. The deep X-ray image shows that the bright compact X-ray source appears to be at the end of a long (25") and slightly curved filament that extends to south (see the top right panel of Figure 3). The compact radio source GCCR056 is embedded in extended radio source M, which also has a filamentary component (Yusef-Zadeh & Morris 1987), but the long ( $\sim$ 20") radio filament is oriented toward the northwest (Zhao et al. 2016), so that the angle between the X-ray and radio filaments is about 120°.

GCCR057.—This source is located 3" SW of GCCR056 and coincides with a compact X-ray source at the tip of a linear feature that appears only in the Muno et al. (2008) catalog of extended X-ray sources; see the top right panel of Figure 3. The linear X-ray source, G359.933-0.037, has a power-law spectrum of  $\Gamma=1.59$  and an X-ray luminosity of  $3\times10^{32}$  erg s<sup>-1</sup>, which is one of the 20 suggested PWNs within the central 20 pc (Muno et al. 2008).

GCCR058.—This radio source appears to be associated with a compact X-ray source surrounded by extended emission source, G359.941-0.029 (Muno et al. 2008). The authors report a power-law spectrum of  $\Gamma=0.44$  and an X-ray luminosity of  $2\times 10^{32}\,\mathrm{erg}\,\mathrm{s}^{-1}$ . The X-ray source is one of the 20 suggested PWNs within the central 20 pc (Muno et al. 2008).

GCCR072.—This is the X-ray counterpart CXOGC J174528.8-285726 (Muno et al. 2009), offset by <0."4 from the radio source, and is also listed as SS#852 in the X-ray catalog of Zhu et al. (2018). The system is interpreted as an O star in a colliding-wind binary (CWB) or high-mass X-ray binary (HMXB) based on IR spectroscopy (DeWitt et al. 2013).

GCCR089.—This is the X-ray counterpart CXOGC J174545.5-285828 (Muno et al. 2009). The compact X-ray source is associated with an extended X-ray source that is interpreted as a PWN (Park et al. 2005). See the central panel of Figure 3. The radio emission from the PWN was described by Zhao et al. (2013). The compact source in both X-ray and radio likely emanates from near the NS (Park et al. 2005; Zhao et al. 2013).

GCCR099.—This radio source may be associated with a faint X-ray component in the diffuse X-ray source, G359.925-0.051

(see the top middle panel of Figure 3). It is interpreted as a PWN (Muno et al. 2008). It is located  $\sim 1''$  NE of GCCR047 (see Figure A1 and Figure 3).

GCCR106.—This source is located 2" NW of GCCR057 and may be also associated with the candidate PWN, G359.933-0.037 (Muno et al. 2008). See the top right panel of Figure 3.

GCCR107.—This source coincides (with an offset <0."5) with the X-ray source CXOGC J174536.1-285638/SS#1671 (Muno et al. 2009; Zhu et al. 2018). An investigation of the X-ray observations of the compact X-ray source implies an apparent  $189 \pm 6$  day periodicity present in the light curve (Mikles et al. 2008). The system is likely associated with an HMXB (Mikles et al. 2008) or with a CWB based on its IR spectrum (Clark et al. 2009). A spectral type of WN8-9h is suggested for the donor star (Mauerhan et al. 2010).

GCCR110.—The X-ray counterpart CXOGC J174532.7-285617/SS#1263 (Mauerhan et al. 2010; Zhu et al. 2018) is offset by <0."7 from the compact radio source. Near infrared spectroscopy implies that the system is associated with a spectral type O4-6I star (Mauerhan et al. 2010).

# 5. Astrophysical Implications

#### 5.1. Spatial Distribution and Extragalactic Contribution

The GCCR sources appear to be mainly distributed along the Galactic plane (Figure 1), indicating that a significant fraction of the compact radio sources are located in the RBZ at the GC. However, at the tens of  $\mu$ Jy level, the density of background extragalactic radio sources becomes noticeable. For example, the VLA deep observations at 5 GHz of the Great Observatories Origins Deep Survey–North (GOODS-N) ( $\sigma_{\rm rms}=3.5~\mu$ Jy beam<sup>-1</sup>, synthesized beam of 1."47 × 1."42) and GOODS-S ( $\sigma_{\rm rms}=3.0~\mu$ Jy beam<sup>-1</sup>, with a beam of 0."98 × 0."45) fields found that these two fields contain 52 and 88 sources over areas of 109 and 190 arcmin², respectively (Gim et al. 2019). The average source density in these two fields above a flux density of 15  $\mu$ Jy is therefore ~0.5 sources arcmin<sup>-2</sup>.

From Table 2, a total of 83 GCCR sources are found in a 45  $\rm arcmin^2$  region within the HPBW of the PB, excluding the area of 3  $\rm arcmin^2$  covered by the Sgr A West and Sgr A East HII regions. The density of GCCR sources above the 70  $\,\mu$ Jy cutoff is therefore  $\sim$ 1.8 sources arcmin<sup>-2</sup>. If we use our GCCR cutoff of 70  $\,\mu$ Jy to recount the sources listed in the GOODS-N and GOODS-S catalog (Gim et al. 2019), the number of sources in the GOODS-N and GOODS-S surveys drops to 46, lowering the source density to 0.15 sources arcmin<sup>-2</sup>. Therefore, the density of GCCR sources revealed by our search is an order of magnitude higher than that found in the GOODS-N and GOODS-S fields.

We note that the extragalactic source density of 0.15 sources  $\arcsin^{-2}$  at 5 GHz derived from the GOODS-N and GOODS-S fields is consistent with that of  $\sim$ 0.1 sources  $\arcsin^{-2}$  for extragalactic background sources above 100  $\mu$ Jy at 3 GHz based on the derived source density by Condon et al. (2012). Of course, the extragalactic background contribution is a function of the distance from the pointing center, for a given flux density cutoff, because it takes a stronger source to appear above the limit out at the edge of RBZ. In conclusion, we find that, at most, about 10% of the GCCR sources are expected to be associated with the extragalactic background population.

Histograms of GCCRs vs nearby MCVs

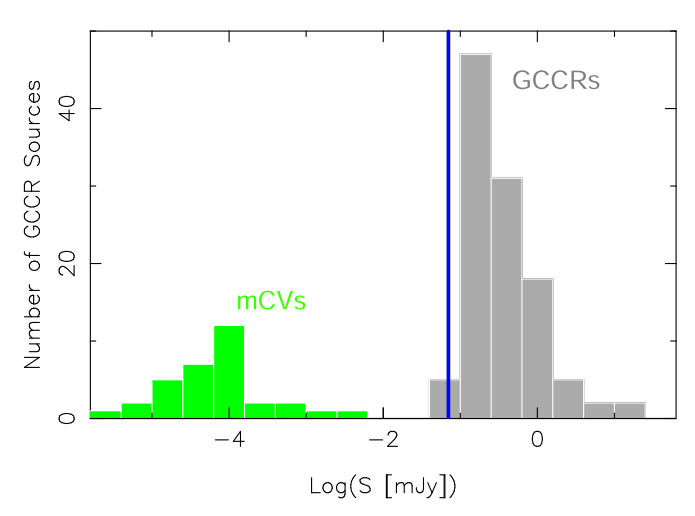


**Figure 4.** Flux density distributions of GCCR sources (gray) vs. the 33 nearby mCVs (green) detected with the VLA (Barrett et al. 2020). The flux densities of the mCVs in this histogram are from JVLA observations at frequencies between 4.5 and 22.1 GHz, extrapolated to the GC at D = 8 kpc assuming a flat spectrum with  $\alpha=0$ . The blue vertical line marks the flux density cutoff for GCCR sources, 70  $\,\mu$ Jy.

#### 5.2. Flux Density Distribution and Cataclysmic Variables

The GC hosts a large population of CVs that are associated with hard X-ray sources (e.g., Muno et al. 2004). In a recent JVLA survey for radio emission from CVs, Barrett et al. (2017, 2020) reported new detections of 33 magnetic CVs, or mCVs, with flux density in the range from 6 to 8031  $\mu$ Jy at frequencies ranging between 4.5 and 22.1 GHz, increasing the number of radio sources associated with CVs to 40. The radio emission of the mCVs is circularly polarized (Barrett et al. 2020) with relatively flat spectra (Barrett et al. 2017). Most of the radio CVs are nearby, at distances ranging from 88 pc to 2.24 kpc, spanning a radio luminosity range from  $3 \times 10^{24} \, \mathrm{erg \, s^{-1}}$  to  $1.7 \times 10^{27} \, \mathrm{erg \, s^{-1}}$ .

To compare the flux density distribution of the radio CVs with our GCCR sources, we scaled the radio flux density of CVs to the GC by multiplying by  $(D/8 \text{ kpc})^2$ . Figure 4 shows a histogram of the radio source counts as a function of radio flux density in the logarithmic range between -5.8 and 1.8, corresponding to a range of flux density between 1.6 nJy  $(10^{-6} \text{ mJy})$  and 63 mJy at a distance of 8 kpc; the logarithm of flux density,  $\log(S \text{ [mJy]})$ , is binned into  $\Delta \log(S \text{ [mJy]}) = 0.4$  intervals starting from -5.8 (1.6 nJy).

The gray histogram in Figures 4 and 5 shows a peak of 47 GCCR sources between -1 and -0.6 in log(S [mJy]). No overlap in flux density is found between the population of detected mCVs (green) and our reported sample of GCCR sources (gray).

The source counts below -1 ( $100 \, \mu \mathrm{Jy}$ ) appear to be incomplete because only a small fraction of the GCCR candidates in the  $\log(S \, [\mathrm{mJy}]) = -1.2$  bin lie above our 70  $\, \mu \mathrm{Jy}$  cutoff marked by the blue vertical line in Figure 4. In spite of the cutoff, the logarithmic flux density distribution of the GCCR population shows a large dispersion, with an average of  $\mu_{\mathrm{Log}(S[\mathrm{mJy}])} = -0.44$  and an rms of  $\sigma_{\mathrm{Log}(S[\mathrm{mJy}])} = 0.47$ . The high-intensity tail of the distribution suggests that the distribution of GCCR sources may consist of multiple Gaussian or *normal* distributions of different source types. However, we cannot rule out the possibility that the GCCR

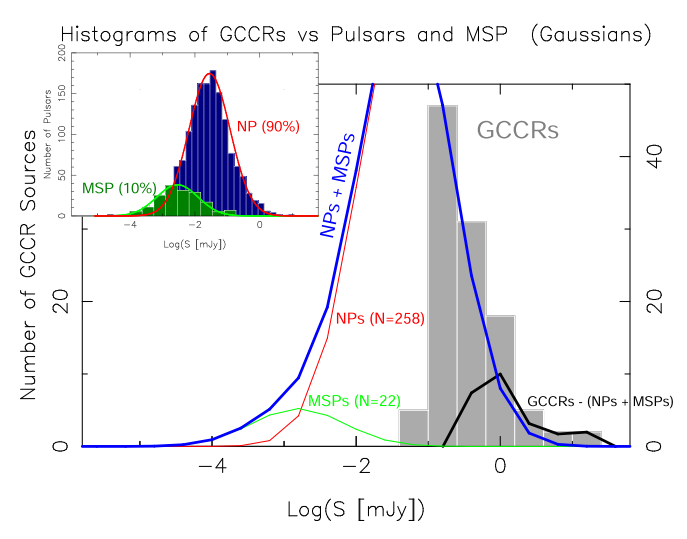


Figure 5. Flux density distribution of GCCR sources (gray histogram) fitted with a sample of 258 NPs (red Gaussian curve) and 22 MSPs (green Gaussian curve), which is 70% of the GD NP and MSP sample used in Kramer et al. (1998). The blue curve is the sum of the two Gaussians. The black curve denotes the difference between counts of the GCCR distribution (gray histogram) and those of the distribution (the blue curve) that is extrapolated from the population of NPs and MSPs in the GD. The 1.5 GHz flux densities of the NPs and MSPs from the samples of Kramer et al. (1998) have been scaled to the flux densities at 5.5 GHz assuming  $\alpha = -1.7$ . The Kramer et al. (1998) sample has also been scaled to the GC distance by scaling their flux densities by  $[1 \text{ kpc/8 kpc}]^2$ . The top left inset shows the distributions of 1503 NPs (darkblue histogram) and 169 MSPs (dark-green histogram) based on a large sample observed at 1.4 GHz (Manchester et al. 2005). The 1.4 GHz flux densities have also been scaled to the flux densities at 5.5 GHz in the GC assuming  $\alpha = -1.7$ and the GC distance of 8 kpc. The red (NPs) and green (MSPs) curves show the fitted Gaussian distributions with  $\mu_{\rm NP}=-1.3$  and  $\mu_{\rm MSP}=-2.5$ , as well as a common standard deviation of  $\sigma = 0.64$ .

population shows an abnormal distribution of the compact radio sources.

# 5.3. Normal Pulsars and MSPs at the Galactic Center

We consider here the possibility that some of the GCCR sources could be pulsars. While the present formation rate of massive stars in the GC is large enough to give rise to the expectation that pulsars would be abundant in the GC, very few are known, presumably because the foreground scatter broadening toward the GC (e.g., Spitler et al. 2014) leads in most cases to a sufficiently large pulse broadening that the pulses become indistinguishable. However, with sufficient sensitivity, pulsars can be detected as point-like continuum radio sources or as PWNe.

A comparison of luminosities and spectral indices between samples of NPs and MSPs has been conducted by Kramer et al. (1998) based on 31 MSPs and 369 NPs distributed in the GD (see also Taylor et al. 1993; Lorimer et al. 1995). They showed that NPs and MSPs have similar spectra, with spectral indices of  $\alpha = -1.6 \pm 0.04$  and  $\alpha = -1.8 \pm 0.1$ , respectively. In addition, the MSPs are an order of magnitude less luminous than NPs. A mean value of  $\log(S\ d^2\ [\text{mJy kpc}^2])$ ,  $\mu_{\text{MSP}} = 0.5 \pm 0.2$  at  $\sim 1.5\ \text{GHz}$ , is derived for MSPs as compared to  $\mu_{\text{NP}} = 1.5 \pm 0.04$  for the NPs (Kramer et al. 1998). As noted by Kramer et al. (1998), the statistics may be subject to a bias owing to the fact that most NPs were discovered in surveys at higher frequencies (that correspondingly selected flatter spectrum and more luminous pulsars), and that most MSPs were discovered at low frequencies and were therefore relatively nearby, subject to

limitations in dispersion removal. To avoid possible statistical bias caused by the difference in the observed luminosities of MSPs and NPs, Kramer et al. (1998) investigated a statistically complete sample of nearby MSPs and NPs. They demonstrated that the discrepancy of the mean values between MSPs and NPs becomes small in the case of restricting to a nearby population within a distance of 1.5 kpc. They find that the mean values of  $\mu_{\rm MSP}$  and  $\mu_{\rm NP}$  are 0.0  $\pm$  0.1 and 0.57  $\pm$  0.09 at  $\sim$ 1.5 GHz, respectively, in a nearby population of 18 MSPs and 55 NPs after removing the apparent biases.

However, the nearby sample excludes the high-luminosity NPs and MSPs that may make a significant contribution to the GCCR population. We would need a large number of pulsars  $(\sim 3000)$  to fit the upper tail of the GCCR distribution if we scaled the nearby sample of Kramer et al. (1998) to the GC. The GD population appears to be more relevant to the distribution of GCCR sources. Using the spectral index  $\alpha = -1.7$  for both MSPs and NPs and a distance of 8 kpc for the GC, we extrapolated the mean values of  $\mu_{MSP}$  and  $\mu_{NP}$ at 1.5 GHz of the GD population of MSPs and NPs to the corresponding values at 5.5 GHz for the GC population, giving  $\mu_{\rm MSP} = -2.3 \ (5 \ \mu {\rm Jy}) \ {\rm and} \ \mu_{\rm NP} = -1.3 \ (50 \ \mu {\rm Jy}) \ {\rm at} \ 5.5 \ {\rm GHz}.$ We then compare the extrapolated GD populations of 369 NPs and 31 MSPs to the distribution of GCCR sources in Figure 5, by approximating the pulsar distributions as Gaussian with a common standard deviation of  $\sigma = 0.64$ ; the value of  $\sigma$  was estimated from the FWHM of the NPs' distribution in  $\log(S \ d^2[\text{mJy kpc}^2])$  (Figure 2 of Kramer et al. 1998). Therefore, on the tentative assumption that all the GCCR sources in the 100-250  $\mu$ Jy bin are pulsars, except for the 10% of them expected to be extragalactic sources, a total of 22 MSPs and 258 NPs would be needed to account for the GCCR distribution. Namely, 70% of the GD population, used in the Kramer et al. (1998) analysis, would be required to match the 47 GCCR sources detected in the log(S [mJy]) =-1 bin covering the flux density range 100–250  $\mu$ Jy.

We further inspected and verified the statistics of Kramer et al. (1998) with a large sample of 1672 pulsars observed at 1.4 GHz (Manchester et al. 2005), 90% of which is NPs (spin period P>30 ms) and 10% is MSPs ( $P\leqslant 30$  ms); see the inset of Figure 5. Scaling to the flux densities at 5.5 GHz at the GC distance (D=8 kpc) and assuming  $\alpha=-1.7$ , we derive the mean ( $\mu_{\rm NP}=-1.3$ ) and standard deviation ( $\sigma=0.64$ ) of the logarithmic flux density from the 1503 NPs, which are in good agreement with the corresponding parameters derived from the GD sample of Kramer et al. (1998). The mean logarithmic flux density of MSPs ( $\mu_{\rm MSP}=-2.5$ ) derived from the 169 MSPs is slightly less than the value ( $\mu_{\rm MSP}=-2.3$ ) of the GD sample, indicating that a difference in the mean flux density between NPs and MSPs in the large sample is insignificantly greater than that of the GD sample.

Therefore, the analysis here is consistent with the possibility that up to 80% of the detected GCCR sources could be NPs if the RBZ hosts a total of 280 NPs and MSPs with a distribution in radio luminosity similar to the GD distribution of NPs and MSPs. However, the MSP population essentially makes no contribution to the upper tail of GCCR sources detected in this paper. Of course, the possible number of NPs among the GCCR sources given above is an upper limit, as other classes of sources can also contribute to the GCCR population, notably the X-ray binaries that we discuss below. A first filter for constraining the NP population among the GCCR sources

could be based on spectral index measurements, given the typically steep spectra of NPs ( $\alpha \sim -1.7$ ). We also note that NPs are usually not strongly variable on timescales of 6 yr or shorter (P. Demorest, personal communication) and only 25% of the GCCR sources are nonvariable, so it appears that NPs are, at most, a minor fraction of the GCCR sources. Of course, firmly identifying pulsars requires detection of their pulsed emission. To date, PSR J1745-2900 is the only confirmed pulsar within the RBZ. PSR J1745–2900 was first identified as an X-ray source by the Swift observatory during a flare (Kennea et al. 2013), and pulsed emission with a period of 3.76 s was revealed in follow-up observations by the NuSTAR observatory (Mori et al. 2013). We note that the analysis in this section does not cover the compact radio sources located within Sgr A West and the Sgr A East HII complex. Located  $\sim 3''$ away from Sgr A\*, PSR J1745-2900 is not listed in Table 2, our GCCR catalog. The discovery of PSR J1745-2900, the GC magnetar, raises the possibility that it might be possible to detect pulsed emission from some of the GCCR sources.

# 5.4. X-Ray Binaries

By comparing the GCCR sources in our 5.5 GHz image with published catalogs of X-ray sources based on observations with the Chandra X-ray observatory and with the Chandra X-ray image from Zhu et al. (2018), we find about 42 possible X-ray counterparts to the GCCR sources (Figure 3). The GCCR sources identified with X-ray counterparts could be close binary systems in which a compact stellar remnant accretes mass from its companion.

X-ray binaries can be divided into two major spectral states based on the hardness of their X-ray spectra: soft and hard states. The soft state is dominated by thermal emission from an accretion disk, while the hard state is dominated by the emission from the corona (Coriat et al. 2011). The radio emission in the hard state is usually characterized by a flat or slightly inverted spectrum with a spectral index of  $\alpha \sim 0$ , which can be interpreted as self-absorbed synchrotron emission from a compact jet, similar to those found in extragalactic nuclei (e.g., Blandford et al. 2019). During the soft state, the compact jets are likely to be quenched (e.g., Fender et al. 1999; Coriat et al. 2011). The presence of a strong correlation between radio and X-ray emission during the hard state has been investigated with observations of several X-ray binaries (e.g., Corbel et al. 2000; Migliari & Fender 2006; Coriat et al. 2011; Tudor et al. 2017; Gallo et al. 2018; Qiao & Liu 2019), showing a power-law relationship  $(L_R \propto L_X^{\beta})$  between the luminosities of X-ray  $(L_X)$  and radio  $(L_R)$ .

For BH X-ray binaries (BHXBs; Fender et al. 2009), the standard value for the power-law index,  $\beta \sim 0.6$  (Corbel et al. 2003, 2008; Gallo et al. 2003; Xue & Cui 2007; Coriat et al. 2011), is thought to be related to the inner region of the accretion system where a hot and inefficient accretion flow (i.e., an advection-dominated accretion flow, or ADAF) might be present (Narayan & Yi 1994; Narayan et al. 1997; Abramowicz & Fragile 2013). The ADAF model appears to reasonably account for sources in the hard state, while the radio emission is optically thick and is correlated with X-ray emission. On the other hand, a steady, powerful, relatively low bulk velocity or bulk Lorentz factor  $\Gamma < 2$  jet is always present in the hard X-ray state (Fender et al. 2009). The observed jets imply a combination of radiatively inefficient flows with the simultaneous presence of MHD winds or outflows. That is,

advection-dominated inflow-outflow solutions, or ADIOS (Blandford & Begelman 1999), may work for the BHXBs.

Similar power-law correlations between  $L_X$  and  $L_R$  are also shown by NS X-ray binaries (NSXBs), but BHXBs are more radio-loud by a factor of 20-30 (Gallo et al. 2018; Kylafis et al. 2012). In a study of disk-jet coupling in low-luminosity accreting NSs in LMXBs, Tudor et al. (2017) show  $L_{\rm R} \propto L_{\rm X}^{\beta}$  relations characteristic of three different types of NSs as compared to the standard relation  $\beta \sim 0.6$  for BHXBs. Transitional MSPs (tMSPs) show  $\beta \sim 0.6$ , the same as that for BHXBs but with an order of magnitude less luminosity at 5 GHz than BHXBs. Nonpulsing NSs correspond to  $\beta \sim 0.7$ , while hard-state NSs have  $\beta \sim 1.4$  (Tudor et al. 2017). It is worth mentioning that the data used in their analysis span six orders of magnitude in 5 GHz radio luminosity ( $L_{5 \text{ GHz}}$ :  $10^{25-31}$  erg s<sup>-1</sup>) and nine orders of magnitude in the 1–10 keV X-ray luminosity ( $L_{\text{X}}$ :  $10^{30-39}$  erg s<sup>-1</sup>.) The BHXBs are mainly distributed in the range of  $L_{5 \text{ GHz}}$  ( $10^{28-31}$  erg s<sup>-1</sup>) along the power-law correlation curve  $(L_{5\,\mathrm{GHz}} \propto L_{\mathrm{X}}^{0.6})$ , while the NSXBs are clustered in a domain around  $10^{27}$ – $10^{29}\,\mathrm{erg\,s^{-1}}$  in  $L_{5\,\mathrm{GHz}}$  and a few times  $10^{36}$ – $10^{37}\,\mathrm{erg\,s^{-1}}$  in  $L_{\mathrm{X}}$ . For X-ray binaries having luminosities in the range of  $10^{36}$ – $10^{37}\,\mathrm{erg\,s^{-1}}$ , the BHXBs appear to be distinguishable from the counterpart NSXBs based on their much higher radio luminosities.

We carried out a regression analysis for the cross-correlation between logarithmic radio and X-ray luminosities for the 42 GCCR sources with X-ray counterparts. The radio luminosities are derived from the flux densities  $S_{\nu}$  given in Table 2 using the form  $L_{\nu} = 4\pi D^2 \nu S_{\nu}$  and  $\nu = 5.5$  GHz. The X-ray luminosities are derived from the photon flux values  $S_{2-8 \text{ keV}}$ , listed in Table 3, provided in the Chandra X-ray catalogs (Muno et al. 2009, 2008; Zhu et al. 2018) using the form  $L_{2-8 \text{ keV}} =$  $4\pi D^2 S_{2-8 \text{ keV}} f_{2-10 \text{ keV}}$ , where  $f_{2-10 \text{ keV}}$  is a photon flux-to-energy conversion factor. We adopted  $f_{2-10 \text{ keV}} = 2.38 \times 10^{-8} \text{ erg}$ photon<sup>-1</sup> (Zhu et al. 2018) to compute the 2–10 keV unabsorbed energy flux. Figure 6 shows a plot of  $L_{5.5 \text{ GHz}}$  versus  $L_{2-10 \text{ keV}}$ for the 42 GCCR sources with X-ray counterparts. We performed a least-squares regression analysis assuming a linear relationship between the logarithmic radio and X-ray luminosities,  $\log(L_{5.5 \text{ GHz}} [\text{erg s}^{-1}]) = \alpha + \beta \log(L_{2-10 \text{ keV}} [\text{erg s}^{-1}]).$ We find that  $\alpha = 7.7 \pm 0.45$  and  $\beta = 0.67 \pm 0.02$  with a correlation coefficient R = 0.72 and a probability of no correlation P < 0.01%. The  $\beta$  value derived for the GCCR sources appears to be consistent with the power-law relationships that are found for BHs, tMSPs, and nonpulsating NSs in the LMXB sample used in the analysis of Tudor et al. (2017).

We also note that the 5.5 GHz radio luminosities of the GCCR sources with X-ray counterparts are in the luminosity range of  $10^{28}$ – $10^{31}$  erg s<sup>-1</sup>, consistent with the range of 5 GHz radio luminosities of the BHXBs used in the analysis of Tudor et al. (2017). However, about 20 GCCR sources with X-ray counterparts having 5.5 GHz radio luminosities below  $1 \times 10^{29} \,\mathrm{erg \, s^{-1}}$ could be explained as NSXBs. The five radio morphology types (given in Column (12) of Table 2) of the GCCR sources are also consistent with the possibility that the compact radio cores are produced from either BHXBs or NSXBs. If the compact cores of the GCCR sources are associated with jet flows from the inner region of accretion disks or from the corona of compact objects, their radio spectra are expected to be flat (Coriat et al. 2011). In addition, a fraction of GCCR sources associated with pulsars and MSPs discussed in Section 5.3 may belong to the category of NSXBs, if they are binaries emitting X-rays. However, some of the GCCR sources with X-ray counterparts listed in Table 3 may

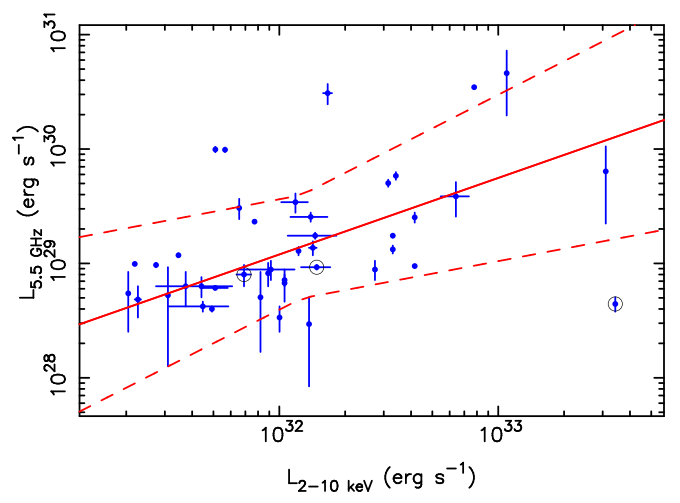


Figure 6. Plot showing the cross-correlation between X-ray and radio luminosities for the 42 GCCR sources having X-ray counterparts. The radio luminosities are derived from the flux densities at 5.5 GHz given in this paper, and the X-ray luminosities are derived from the X-ray photon fluxes in the 2–8 keV X-ray band reported in the X-ray catalogs (Muno et al. 2008, 2009; Zhu et al. 2018). The black circles mark the three candidate HMXBs (Section 4.2). The red solid line is the result from a least-squares fit to the logarithmic X-ray and radio luminosities, implying a power-law relation  $L_{5.5\,\mathrm{GHz}} \propto L_{2-10\,\mathrm{keV}}^{\beta}$ . The red dashed lines outline the range in which the true regression line lies at a confidence level of 95%, derived with Scheffé's method (https://en.wikipedia.org/wiki/Confidence\_and\_prediction\_bands and https://www.itl.nist.gov/div898/handbook/prc/section4/prc472.htm).

just be associated with PWNs powered by a single NS. Further study of the GCCR sources with coordinated radio and X-ray observations will help to distinguish between BHs and NSs for the compact objects associated with the GCCR sources.

Finally, we note the recent detection of a 91  $\pm$  10  $\mu$ Jy source at 5.5 GHz at the position of the GC transient caught during its flare in 1990 (GCT1990) with a flux density then of  $\sim$ 1 Jy at 1.5 GHz (Zhao et al. 1992, 2020), implying  $L_{5.5\,\mathrm{GHz}}=2\times10^{32}\,\mathrm{erg}\,\mathrm{s}^{-1}$  during the 1990 flare. This GCCR source is located within the Sgr A West region, which does not match the selection criteria used to compile Table 2, so the GCT1990 is not included in the above analysis. If this radio source is a remnant or the impact site of the compact jet of GCT1990 that has been quenched as the source transitioned from a hard state to the soft state, then the quenching factor of the GCT1990 is  $\sim$ 5000, an order of magnitude greater than that of H1743-322 (Coriat et al. 2011). The high radio luminosity during the outburst of 1990 is consistent with the hypothesis of a BHXB for the GCT1990 (Zhao et al. 1992), although the possibility of an NSXB cannot be completely ruled out.

#### 6. Conclusion

We imaged the RBZ with wide-band continuum data taken at 5.5 GHz with the VLA in its A array at three epochs: 2019 September 8, 2014 May 17, and 2014 May 26. A total of 110 GCCR sources have been detected at an angular resolution of 0."4 outside Sgr A West and the complex of Sgr A East HII regions. The  $10\sigma$  cutoff in flux density used in the GCCR survey is  $70 \mu$ Jy. Five types of sources are classified according to their morphology: (1) an unresolved source, (2) a compact

<sup>11</sup> The quenching factor is defined as a ratio of the peak value of radio flux density during an outburst to the lowest value in the outburst light curve (Coriat et al. 2011).

source with a size determined from 2D Gaussian fitting, (3) a compact source associated with a linear feature, (4) a compact source with a radio tail, and (5) a double compact source.

In general, the GCCR sources are distributed along the Galactic plane, and about 10% of them are expected to be extragalactic background sources. The mean value of logarithmic flux density at 5.5 GHz,  $\mu_{\text{Log}(S[mJy])} = -0.44$  with a standard deviation of  $\sigma_{\text{Log}(S[mJy])} = 0.47$ , suggests that the GCCR sources are at least three orders of magnitude more luminous than the radio sources powered by magnetic CVs, i.e., close binaries containing a WD. On the other hand, when compared to the GD population of NPs, a majority (80%) of the GCCR sources appears to fall within the high flux density tail of the pulsar distribution, as extrapolated from a sample of NPs in the GD. However, MSPs extrapolated from the GD population are too weak to have contributed significantly to the GCCR population that has been detected.

We also cross-correlated the GCCR sources with X-ray sources in Chandra X-ray catalogs and found that 42 GCCR sources have candidate X-ray counterparts. In addition, our regression analysis shows that the logarithmic X-ray ( $L_{2-10~\rm keV}[{\rm erg~s}^{-1}]$ ) and radio ( $L_{5.5~\rm GHz}[{\rm erg~s}^{-1}]$ ) luminosities are linearly correlated, with a correlation coefficient of 0.72. The radio luminosities and radio morphologies, along with the compactness of the sources, suggest that the radio emission from the GCCR sources having X-ray counterparts is consistent with compact radio jets launched from X-ray binary systems associated with either a BH or an NS. Some of them are associated with PWNs. Among the GCCR sources with candidate X-ray counterparts, the lower-luminosity ones could include some NSXBs, while those with a higher luminosity are candidate BHXBs.

We are grateful to the anonymous referee and to the editors for providing their valuable comments and suggestions. The Very Large Array (VLA) is operated by the National Radio Astronomy Observatory (NRAO). The NRAO is a facility of the National Science Foundation operated under cooperative agreement by Associated Universities, Inc. The research has made use of NASA's Astrophysics Data System. This research has also made use of the VizieR catalog access tool, CDS, Strasbourg, France (DOI: 10.26093/cds/vizier).

# Appendix The Galactic Center Compact Radio Sources

We catalog the newly detected 110 GCCR sources from the RBZ, covering the central 180 arcmin<sup>2</sup> area. The radio flux densities of individual GCCR sources are determined from the three epochs' observations on 2019 September 8, 2014 May 26, and 2014 May 17. The 110 compact sources listed in Table 2 are divided into two groups: (1) variables or transients (N=82) if  $\Delta S/\sigma \geqslant 4$ , where

$$\Delta S = S_{\text{max}} - S_{\text{min}} \tag{A1}$$

is the range of variation in flux density S and

$$\sigma = \left(\sum_{i=1}^{i=3} \frac{1}{\sigma_i^2}\right)^{-1/2} \tag{A2}$$

is an uncertainty in the average flux density, S; and (2) nonvariables (N = 28) if  $\Delta S/\sigma < 4$ .

#### A.1. A Catalog of the GCCR Sources

Table 2 lists the radio properties of the 110 GCCR sources along with their X-ray identifications.

Column (1) is the source ID for the GCCR sources that are identified from the three epochs' VLA 5.5 GHz images; these images are produced by filtering out the short-spacing uv data and applying the correction for PB attenuation. The three dirty images were cleaned with the MS-MSF algorithm (Rau & Cornwell 2011), and the images with the cleaned components were finally convolved with a common beam of FWHM  $0.750 \times 0.724$  (-0.05). Thus, the intensities of a source observed at the three epochs are not biased by different sizes of their original synthesized beams that are listed in Column (9) of Table 1. A comparison of the source intensities can be carried out for the three epochs. Figure A1 shows the 5.5 GHz, high-resolution contour images for each of the GCCR sources at the three epochs displayed in the same column: panel (a) for 2019 September 8, panel (b) for 2014 May 26, and panel (c) for 2014 May 17. The images were made with the MS-MFS algorithm (Rau & Cornwell 2011), averaging every two channels with a resultant channel bandwidth of 4 MHz.

Column (2) gives the equatorial coordinates of the sources at the epoch of J2000. The uncertainty in position presuambly dominated by thermal noise is  $\sigma_{\theta} = 0.5\theta_{\text{beam}}(\text{S/N})^{-1}$ , where  $\theta_{\text{beam}}$  is the FWHM of a telescope beam and S/N is the ratio of signal to noise. Given a synthesized beam of  $\theta_{\rm beam} \sim 0.6$ , elongated nearly in N-S, and minimum S/N of 10, the positional uncertainties in R.A. and decl. are  $\sigma_{\alpha} \lesssim 0.002^{s}$  and  $\sigma_{\delta} \lesssim 0.03$ , respectively. However, a source located far from the phase center of the interferometer array is subject to a BWS effect<sup>8</sup>. Thus, the clean beam is smeared by a Gaussian in the radial direction, with an FWHM proportional to  $\frac{\delta \nu}{\nu_0} r_{\theta}$ . For a source located at the edge of the field  $r_{\theta} \sim 450''$ , the quantity  $\frac{\delta \nu}{r_{ heta}} r_{ heta} \sim 0\rlap.{''}32$  represents the largest angular size caused by the BWS effect corresponding to the ratio of channel width to band center frequency  $\frac{\delta \nu}{\mu} = 7 \times 10^{-4}$ . Convolving  $\theta_{\text{beam}}$  with the FWHM of the BWS effect, the resulting beam will increase by a factor of <1.13, depending on  $\frac{\delta \nu}{\mu_0} r_{\theta}$ .

Column (3) lists the angular distance  $r_{\theta}$  of a GCCR source with respect to the phase center  $(\alpha_{\rm p}, \delta_{\rm p})$  for given GCCR source R.A. and decl.  $(\alpha, \delta)$  based on the following equation:

$$\cos(r_{\theta}) = \cos(\delta)\cos(\delta_{p}) + \sin(\delta)\sin(\delta_{p})\cos(\alpha - \alpha_{p}).$$
 (A3)

Columns (4) and (5) give the angular offsets in R.A. and decl. with respect to Sgr A\*.

Column (6) lists the PB correction factor  $\mathcal{F}_{PB} = A(x)^{-1}$ .

Column (7) gives  $\sigma \mathcal{F}_{PB}^{-1} = \sigma_A A(x)^{-1}$ , corresponding to the fractional uncertainty of the PB correction. The uncertainty  $\sigma_A$  of A(x) is computed with Equation (2).

As a consequence of the BWS effect of stretching the synthesized beam, the apparent peak intensity of a source decreases, while the source flux density remains invariant. The source intensity is reduced by a factor of  $\sqrt{1 + \beta^2}$ , where

$$\beta = \frac{\delta \nu}{\nu_0} \frac{r_\theta}{\theta_{\text{beam}}} \tag{A4}$$

for an FWHM synthesized beam  $\theta_{\text{beam}}$  (Bridle & Schwab 1999). For a 2D Gaussian source, the flux density S of a source is a linear function of the apparent peak intensity  $S_p$  and angular



Figure A1. Contour plots for individual GCCR sources at epochs (a) 2019 September 8, (b) 2014 May 26, and (c) 2014 May 17. Each of the sources is arranged in the same column labeled with its GCCR ID number at top. Contours are  $\sigma_{\text{map}} \times (-5, 5 \times \sqrt{2^n})$ , where n = -1, 0, 1, 2, 3, 4, 5 ... until reaching the intensity peak. The rms noises  $\sigma_{\text{map}}$  are listed in Column (11) in Table 2 for corresponding GCCR sources. For the panels of Sgr A\*,  $\sigma_{\text{map}} = 10$  mJy beam¹, 100 times greater than the local rms noise near the source. The coordinate labels are the angular offsets from the phase center of the date or the pointing center of the VLA observations; the coordinates of the phase center are given in the text<sup>6</sup>.

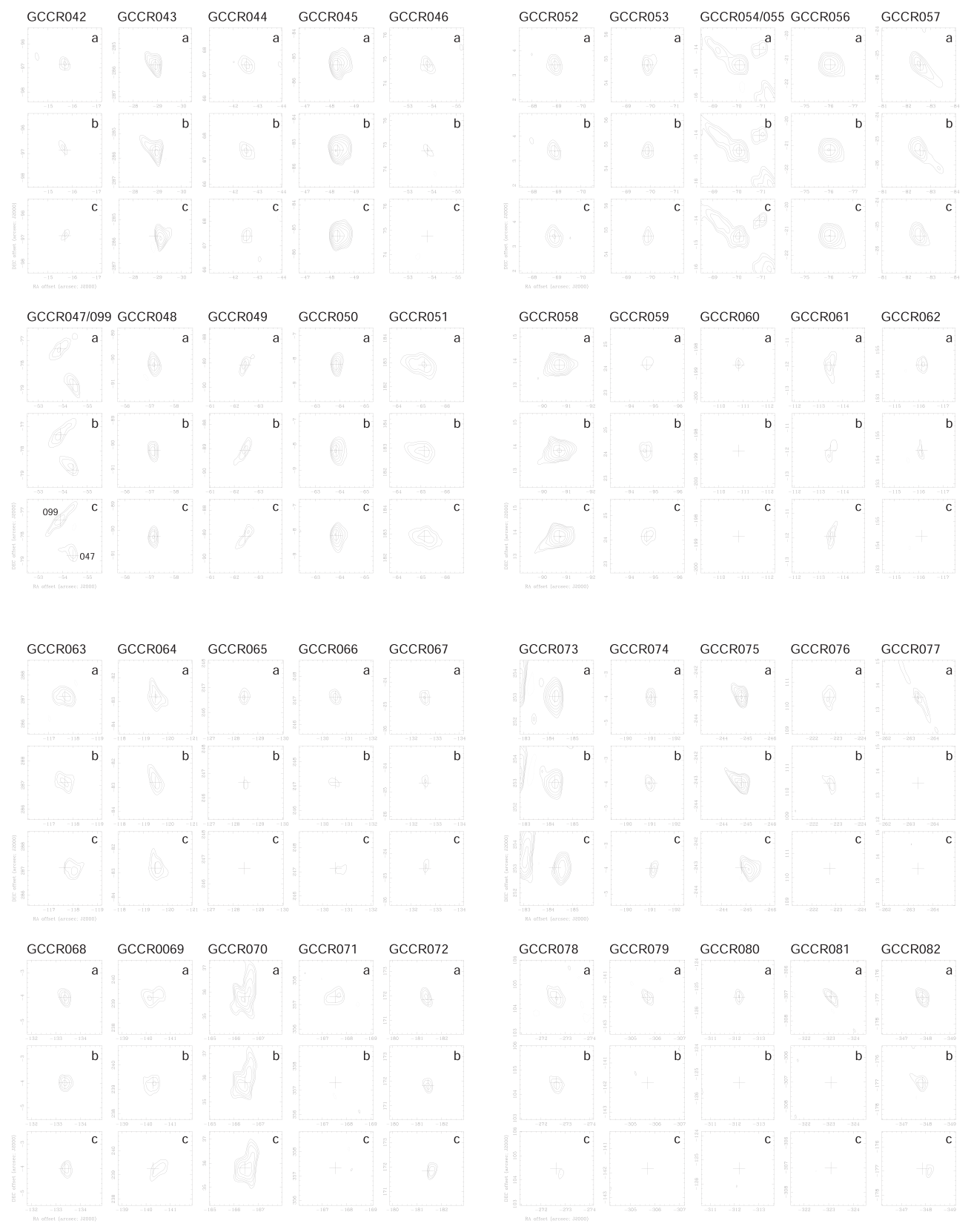


Figure A1. (Continued.)



Figure A1. (Continued.)

size  $\Theta_{\text{FWHM}}$ ,

$$S = \frac{\pi S_{\rm p}}{4\ln(2)} \Theta_{\rm FWHM}.\tag{A5}$$

The apparent angular size  $\Theta_{\rm FWHM}$  is a resultant of the source intrinsic size  $(\theta_{\rm maj} \times \theta_{\rm min})$  convolved with a telescope beam. In principle, the smearing effect reduces  $S_{\rm p}$  and enlarges  $Q_{\rm FWHM}$  but does not change S. The AIPS task JMFIT provides an option for correcting the BWS effect while fitting a 2D Gaussian function to a compact source. The flux densities S along with the uncertainties S due to the rms noise are reported in Columns (8)–(10), corresponding to the measurements at epochs 2019 September 08, 2014 May 26, and 2014 May 17.

Column (11) provides the rms  $\sigma_{\text{map}}$  in the regions near the sources that are plotted in contours; see Figure A1.

Column (12) gives classifications of the GCCR sources. Five types of sources are classified according to their morphology: u-core stands for unresolved compact source, c-core is for a compact source with a size determined from 2D Gaussian fitting, l-core is for a compact source associated with a linear feature, t-core is for a compact source having a tail, and d-core is for a double compact source. The results derived from 2D Gaussian fitting for intrinsic sizes  $\theta_{\rm maj}$  and  $\theta_{\rm min}$ , as well as position angle PA, are given in the notes for corresponding individual sources for all the GCCR types other than u-core.

Column (13) provides a brief note for the X-ray identifications. The code "y" stands for the GCCR sources that are identified with X-ray counterparts with a positional offset between X-ray and radio less than 1" ( $\Delta\theta_{X-R} < 1$ ") or located in the inner region of an X-ray halo; the code "y?" means that a possible X-ray counterpart is present near the GCCR sources or

 $\Delta\theta_{X-R}=1''$  to 2" for the offsets between the GCCR sources and X-ray candidates; the letter "n" means that no X-ray counterparts have been identified for the GCCR sources with  $\Delta\theta_{X-R}>2''$ . The procedure to identify X-ray counterparts for the GCCR sources was based on cross-examinations between the Chandra X-ray and VLA 5.5 GHz images in addition to searching the online catalogs of the X-ray sources at the GC (Muno et al. 2008, 2009; Zhu et al. 2018) for the GCCR sources' X-ray counterparts as described in Section 4.

# ORCID iDs

Jun-Hui Zhao https://orcid.org/0000-0002-1317-3328 Mark R. Morris https://orcid.org/0000-0002-6753-2066 W. M. Goss https://orcid.org/0000-0001-6596-8803

#### References

```
Abramowicz, M. A., & Fragile, P. C. 2013, LRR, 16, 1
Aharon, D., & Perets, H. B. 2015, ApJ, 799, 185
Aizu, K. 1973, PThPh, 50, 344
Antonini, F., Barausse, E., & Silk, J. 2015, ApJ, 812, 72
Arca-Sedda, M., & Capuzzo-Dolcetta, R. 2017, MNRAS, 471, 478
Barrett, P. E., Dieck, C., Beasley, A. J., et al. 2017, AJ, 154, 252
Barrett, P. E., Dieck, C., Beasley, A. J., Mason, P. A., & Singh, K. P. 2020,
   AdSpR, 66, 1226
Bates, S. D., Johnston, S., Lorimer, D. R., et al. 2011, MNRAS, 411, 1575
Bird, A. J., Bazzano, A., Malizia, A., et al. 2016, ApJS, 223, 15
Blandford, R., Meier, D., & Readhead, A. 2019, ARA&A, 57, 467
Blandford, R. D., & Begelman, M. C. 1999, MNRAS, 303, L1
Bower, G. C., Chatterjee, S., Cordes, J., et al. 2018, in ASP Conf. Ser. 517,
   Science with a Next Generation Very Large Array, ASP Monograph 7, ed.
   E. Murphy (San Francisco, CA: ASP), 793
Bower, G. C., Deller, A., Demorest, P., et al. 2014, ApJL, 780, L2
Bridle, A. H., & Schwab, F. R. 1999, in ASP Conf. Ser. 180, Synthesis
   Imaging in Radio Astronomy II, ed. G. B. Taylor, C. L. Carilli, &
   R. A. Perley (San Francisco, CA: ASP), 371
Brook, P. R., Karastergiou, A., McLaughlin, M. A., et al. 2018, ApJ, 868, 122
Clark, J. S., Crowther, P. A., & Mikles, V. J. 2009, A&A, 507, 1567
Condon, J. J., Cotton, W. D., Fomalont, E. B., et al. 2012, ApJ, 758, 23
Coppejans, D., & Knigge, C. 1919, To appear in New Astronomy Reviews
   special volume '100 Years of Astrophysical Jets, ed. R. Fender & R. Wijers,
   arXiv:2003.05953
Corbel, S., Fender, R. P., Tzioumis, A. K., et al. 2000, A&A, 359, 251
Corbel, S., Kr"ding, E., & Kaaret, P. 2008, MNRAS, 389, 1697
Corbel, S., Nowak, M. A., Fender, R. P., et al. 2003, A&A, 400, 1007
Coriat, M., Corbel, S., Prat, L., et al. 2011, MNRAS, 414, 677
Degenaar, N., & Wijnands, R. 2010, A&A, 524, A69
Degenaar, N., Wiljnands, R., Miller, J. M., et al. 2015, JHEAp, 7, 137
DeWitt, C., Bandyopadhyay, R. M., Eikenberry, S. S., et al. 2013, AJ, 146, 109
Dexter, J., & O'Leary, R. M. 2014, ApJL, 783, L7
Eatough, R. P., Falcke, H., Karuppusamy, R., et al. 2013a, Natur, 501, 391
Eatough, R. P., Kramer, M., Klein, B., et al. 2013b, Neutron Stars and Pulsars:
   Challenges and Opportunities after 80 years (Cambridge: Cambridge Univ.
Eatough, R. P., Lazio, T. J. W., Casanellas, J., et al. 2015, in Proc. Advancing
   Astrophysics with the Square Kilometre Array (AASKA14) (Trieste:
   SISSA), 45
Ekers, R. D., Goss, W. M., Schwarz, U. J., Downes, D., & Rogstad, D. H.
   1983, A&A, 122, 143
Feldmeier, A., Neumayer, N., Seth, A., et al. 2014, A&A, 570, A2
Fender, R., Corbel, S., Tzioumis, T., et al. 1999, ApJL, 519, L165
Fender, R., Homan, J., & Belloni, T. M. 2009, MNRAS, 396, 1370
Gallo, E., Degenaar, N., & van den Eijinden, J. 2018, MNRAS, 478, L132
Gallo, E., Fender, R. P., & Pooley, G. G. 2003, MNRAS, 344, 60
Genzel, R., Eisenhauer, F., & Gillessen, S. 2010, RvMP, 82, 3121
Ghez, A. M., Salim, S., Hornstein, S. D., et al. 2005, ApJ, 620, 744
Gim, H. B., Yun, M. S., Owen, F. N., et al. 2019, ApJ, 875, 80
Goss, W. M., Schwarz, U. J., van Gorkom, J. H., & Ekers, R. D. 1985,
   MNRAS, 215, 69
Haggard, D., Heinke, C., Hooper, D., & Linden, T. 2017, JCAP, 5, 56
Hailey, C. J., Mori, K., Bauer, F. E., et al. 2018, Natur, 256, 70
Hailey, C. J., Mori, K., Perez, K., et al. 2016, ApJ, 826, 160
```

```
Heard, V., & Warwick, R. S. 2013, MNRAS, 428, 346
Hong, J., Mori, K., Hailey, C. J., et al. 2016, ApJ, 825, 132
Johnston, S., & Kerr, M. 2018, MNRAS, 474, 4629
Johnston, S., Kramer, M., Lorimer, D. R., et al. 2006, MNRAS, 373, L6
Kennea, J. A., Burrows, D. N., Kouveliotou, C., et al. 2013, ApJL, 770, L24
Kramer, M., Klein, B., Lorimer, D., et al. 2000, in ASP Conf. Ser. 202, The
  Effelsberg Search for Pulsars in the Galactic Centre in Pulsar Astronomy—
  2000 and Beyond, ed. M. Kramer, N. Wex, & N. Wielebinski (San
  Francisco, CA: ASP), 37
Kramer, M., Lange, C., Lorimer, D. R., et al. 1999, ApJ, 526, 957
Kramer, M., Lyne, A. G., O'Brien, J. T., Jordan, C. A., & Lorimer, D. R. 2006,
   Sci, 312, 549
Kramer, M., Xilouris, K. M., Lorimer, D. R., et al. 1998, ApJ, 501, 270
Kylafis, N. D., Contopoulos, I., Kazanas, D., & Christodoulou, D. M. 2012,
    &A, 538, A5
Ledlow, M. J., Zeilik, M., Burns, J. O., et al. 1992, ApJ, 384, 640
Lorimer, D. R., Yates, J. A., Lyne, A. G., & Gould, D. M. 1995, MNRAS,
Lu, J. R., Do, T., Ghez, A. M., et al. 2013, ApJ, 764, 155
Macquart, J.-P., & Kanekar, N. 2015, ApJ, 805, 172
Macquart, J.-P., Kanekar, N., Frail, D. A., & Ransom, S. M. 2010, ApJ,
Manchester, R. N., Hobbs, G. B., Teoh, A., & Hobbs, M. 2005, AJ, 129, 1993
Mauerhan, J. C., Muno, M. P., Morris, M. R., Stolovy, S. R., & Cotera, A.
  2010, ApJ, 710, 706
McClintock, R. 2006, ARA&A, 44, 49
Migliari, S., & Fender, R. P. 2006, MNRAS, 366, 79
Mikles, V. J., Eikenberry, S. S., Bandyopadhyay, R. M., & Muno, M. P. 2008,
   ApJ, 689, 1222
Mills, E., Morris, M. R., Lang, C. C., et al. 2011, ApJ, 735, 84
Milosavljević, M. 2004, ApJL, 605, L13
Mori, K., Gotthelf, E. V., Zhang, S., et al. 2013, ApJL, 770, L23
Morris, R. M., Zhao, Jun-Hui, & Goss, W. M. 2017, ApJL, 850, L23
Muno, M. P., Baganoff, F. K., Bautz, M. W., et al. 2003, ApJ, 589, 225
Muno, M. P., Baganoff, F. K., Bautz, M. W., et al. 2004, ApJ, 613, 326
Muno, M. P., Baganoff, F. K., Brandt, W. N., et al. 2008, ApJ, 673, 251
Muno, M. P., Bauer, F. E., Baganoff, F. K., et al. 2009, ApJS, 181, 110
Muno, M. P., Bauer, F. E., Bandyopadhyay, R. M., & Wang, Q. D. 2006,
Muno, M. P., Lu, J. R., Baganoff, F. K., et al. 2005, ApJ, 633, 228
Narayan, R., Garcia, M. R., & McClintock, J. E. 1997, ApJ, 452, 710
Narayan, R., & Yi, I. 1994, ApJL, 428, L13
Oh, K., Koss, M., Markwardt, C. B., et al. 2018, ApJS, 235, 4
Park, S., Muno, M. P., Baganoff, F. K., et al. 2005, ApJ, 631, 964
Perez, K., Hailey, C. J., Bauer, F. E., et al. 2015, Natur, 520, 646
Perley, R. 2016, NRAO EVLA Memo, http://library.nrao.edu/public/
  memos/evla/EVLAM_195.pdf
Perley, R. A., & Bulter, B. J. 2017, ApJS, 230, 7
Pfahl, & Loeb 2004, ApJ, 615, 253
Qiao, Erlin, & Liu, B. F. 2019, MNRAS, 487, 1626
Rajwade, K. M., Lorimer, D. R., & Anderson, L. D. 2017, MNRAS, 471, 730
Rau, U., & Cornwell, T. J. 2011, A&A, 532, A71
Schödel, R., Feldmeier, A., Kunneriath, D., et al. 2014, A&A, 566, A47
Schödel, R., Nogueras-Lara, F., Gallego-Cano, E., et al. 2020, A&A,
  641, A102
Schödel, R., Ott, T., Genzel, R., et al. 2003, ApJ, 596, 1015
Shakura, N. I., & Sunyaev, R. A. 1973, A&A, 24, 337
Spitler, L. G., Lee, K. J., Eatough, R. P., et al. 2014, ApJL, 780, L3
Taylor, J. H., Manchester, R., & Lyne, A. G. 1993, ApJS, 88, 529
Thompson, A. R., Moran, J. M., & Swenson, G. W., Jr. 2017, Interferometry
  and Synthesis in Radio Astronomy (3rd edn.; Berlin: Springer)
Tremaine, S. D., Ostriker, J. P., & Spitzer, L., Jr. 1975, ApJ, 196, 407
Tudor, V., Miller-Jones, J. C. A., Patruno, A., et al. 2017, MNRAS,
  470, 324
van den Eijnden, J., Degenaar, N., Russell, T. D., et al. 2018, Natur, 562, 233
Wharton, R. S., Chatterjee, S., Cordes, J. M., et al. 2012, ApJ, 753, 108
Xue, Y. Q., & Cui, W. 2007, A&A, 466, 1053
Yusef-Zadeh, F., & Morris, M. 1987, ApJ, 320, 545
Zhao, J.-H., Desai, K., Goss, W. M., & Yusef-Zadeh, F. 1993, ApJ, 418, 235
Zhao, J.-H., Morris, M. R., & Goss, W. M. 2013, ApJ, 777, 146
Zhao, J.-H., Morris, M. R., & Goss, W. M. 2016, ApJ, 817, 171
Zhao, J.-H., Morris, M. R., & Goss, W. M. 2019, ApJ, 875, 134
Zhao, J.-H., Morris, M. R., & Goss, W. M. 2020, GCWS2019, ed. T. Masato &
  O. Tomoharu, arXiv:2010.12352
Zhao, J.-H., Roberts, D. A., Goss, W. M., et al. 1992, Sci, 255, 1538
Zhu, Z., Li, Z., & Morris, M. R. 2018, ApJS, 235, 26
```